

Theoretical study of the flow in a fluid damper containing high viscosity silicone oil: effects of shear-thinning and viscoelasticity

Alexandros Syrakos^{a,*}, Yannis Dimakopoulos^a, John Tsamopoulos^a

^aLaboratory of Fluid Mechanics and Rheology, Department of Chemical Engineering, University of Patras, 26500 Patras, Greece

Abstract

The flow inside a fluid damper where a piston reciprocates sinusoidally inside an outer casing containing high-viscosity silicone oil is simulated using a Finite Volume method, at various excitation frequencies. The oil is modelled by the Carreau-Yasuda (CY) and Phan-Thien & Tanner (PTT) constitutive equations. Both models account for shear-thinning but only the PTT model accounts for elasticity. The CY and other generalised Newtonian models have been previously used in theoretical studies of fluid dampers, but the present study is the first to perform full two-dimensional (axisymmetric) simulations employing a viscoelastic constitutive equation. It is found that the CY and PTT predictions are similar when the excitation frequency is low, but at medium and higher frequencies the CY model fails to describe important phenomena that are predicted by the PTT model and observed in experimental studies found in the literature, such as the hysteresis of the force-displacement and force-velocity loops. Elastic effects are quantified by applying a decomposition of the damper force into elastic and viscous components, inspired from LAOS (Large Amplitude Oscillatory Shear) theory. The CY model also overestimates the damper force relative to the PTT, because it underpredicts the flow development length inside the piston-cylinder gap. It is thus concluded that (a) fluid elasticity must be accounted for and (b) theoretical approaches that rely on the assumption of one-dimensional flow in the piston-cylinder gap are of limited accuracy, even if they account for fluid viscoelasticity. The consequences of using lower-viscosity silicone oil are also briefly examined.

This is the accepted version of the article published in:
Physics of Fluids 30, 030708 (2018); doi:[10.1063/1.5011755](https://doi.org/10.1063/1.5011755)

1. Introduction

Viscous dampers are devices that dissipate mechanical energy into heat through the action of viscous stresses in a fluid; such stresses develop because the fluid is forced to flow through a constriction. A common design involves the motion of a piston in a cylinder filled with a fluid, such that large velocity gradients develop in the narrow gap between the piston head and the cylinder, resulting in viscous and pressure forces that resist the piston motion. Viscous dampers are used in a range of applications, including the protection of buildings and bridges from damage induced by seismic and wind excitations [1, 2], and the absorption of shock and vibration energy in vehicles [3, 4] and aerospace structures [5].

A common mathematical model used to describe the behaviour of fluid dampers assumes that the instantaneous damper force F depends only on the instantaneous piston velocity U according to

$$F = CU^n \quad (1)$$

where C is the damping constant and n is an exponent usually in the range 0.3 to 2 [6]. Dampers that conform to the above relationship are characterised as purely viscous dampers. Also, they are classified as

*Corresponding author

Email addresses: syrakos@upatras.gr, alexandros.syrakos@gmail.com (Alexandros Syrakos), dimako@chemeng.upatras.gr (Yannis Dimakopoulos), tsamo@chemeng.upatras.gr (John Tsamopoulos)

linear if $n = 1$ or nonlinear if $n \neq 1$. Although Eq. (1) often describes well the behaviour of fluid dampers in a range of operating conditions, dampers in many cases also exhibit a spring-like behaviour, especially at high frequencies, where the damper force has a component that is in phase with the piston displacement. For linear dampers, a simplifying analysis [1, 6] shows that if a sinusoidal piston displacement $X = X_0 \sin(\omega t)$ is forced upon the damper and the resulting force is at a phase lag with the piston velocity then this force can be expressed as

$$F = C \dot{X} + K X \quad (2)$$

where the dot denotes differentiation with respect to time ($\dot{X} \equiv dX/dt \equiv U$) and K is called the storage stiffness. Equation (2) essentially assumes that the actual damper can be modelled as an ideal linear purely viscous damper connected in parallel with an ideal spring. Alternatively, one can assume these two components to be connected in series, which results in the macroscopic Maxwell model [1]:

$$F + \lambda \dot{F} = C \dot{X} \quad (3)$$

where $\lambda \equiv C/K$ is called the relaxation time of the model. Macroscopic models of the damper behaviour such as (1), (2) and (3) are needed for the prediction of the dynamic response to excitations of structures that incorporate dampers. These and many more such models that have been proposed over time (see e.g. [7–9] and references therein) are mostly phenomenological, i.e. they are not derived from first principles but are empirical relationships. Each model incorporates a number of parameters such as C and λ whose values have to be obtained by fitting the model to experimental data for each particular damper.

The mechanical behaviour of a fluid damper depends on several factors (damper design and dimensions, fluid properties, operating conditions) and to obtain insight into the role of each of these one has to consider the damper operation from first principles. Energy dissipation occurs as the mechanical excitation causes parts of the damper to move relative to each other, forcing fluid through an orifice. Therefore the equations governing fluid flow must be considered. The flow is in general multidimensional and time-dependent, but in several studies simplifications have been made to make it amenable to solution by analytical means or by simple numerical methods. The simplifications commonly made are: (a) that the only important region is that of the orifice; (b) that the orifice is narrow and long so that the flow there can be assumed one-dimensional; and (c) that the flow is quasi-steady, i.e. the effect of the time derivatives in the governing equations can be neglected. These reduce the problem to planar or annular Couette-Poiseuille flow that can be solved to obtain the wall shear stress and pressure gradient, and hence the viscous and pressure force on the piston.

A fluid very commonly employed in dampers, especially those used in civil engineering applications, is silicone oil (poly(dimethylsiloxane) (PDMS) [10–12]). Studies concerning silicone oil dampers include [1, 6, 5, 13–16]. Silicone oil is a polymeric fluid whose long molecules become aligned under shear resulting in a drop of viscosity; this property is called shear-thinning, and is more pronounced in silicone oils of high molecular weight. Due to shear-thinning, the force with which the damper reacts to excitations is significantly lower than what it would be if the fluid viscosity was constant. Therefore, shear-thinning must be accounted for in theoretical studies, and a popular constitutive equation that can describe this sort of behaviour is the Carreau-Yasuda (CY) [17] model. The CY model has been used in [16] for a theoretical study of the flow in a silicone oil damper under the aforementioned simplifying assumptions of one-dimensional flow that render the problem amenable to analytical solution. Two dimensional (axisymmetric) simulations of the whole flow have also been performed, assuming silicone oil to behave as either a Newtonian [14] or a CY fluid [18], using commercial Computational Fluid Dynamics (CFD) solvers.

Silicone oil, like most polymeric fluids, possesses another property, namely elasticity, which is a tendency to partially recover from its deformation. The CY constitutive equation, being of generalised Newtonian type, relates the stress tensor only to the instantaneous rate of strain tensor and hence cannot describe elastic effects, which depend on the flow history. Constitutive equations that predict elastic behaviour are more difficult to solve than generalised Newtonian ones and hence theoretical analyses usually assume elasticity to be negligible and generalised Newtonian models such as CY to be sufficient. Yet, the CY model fails to predict the stiffness aspect of the damper's behaviour mentioned above, and it is natural to wonder whether this stiffness is due to the elasticity of silicone oil. This has been investigated in a couple of theoretical studies employing the one-dimensional flow simplifying assumption [19, 14] which suggest that indeed fluid elasticity is a cause of damper stiffness, although this has been disputed in favour of fluid compressibility

as the cause [20, 16]. A better picture would be obtained by performing simulations of the whole flow using a viscoelastic constitutive equation, and to the best of the authors' knowledge the present study is the first to attempt this. A possible reason for the lack of such prior studies is that viscoelastic simulations are much more expensive than those involving generalised Newtonian fluids such as the CY, as additional differential equations have to be solved (one per stress component), which are unwieldy at high elasticity (the notorious high-Weissenberg number problem – see e.g. [21]), while also much smaller time steps are needed in order to capture the elastic phenomena (whereas if the flow is assumed generalised Newtonian, it is also quasi-steady due to the high viscosity of typical damper fluids and one can employ large time steps without loss of accuracy – see [22]).

In the present paper we present flow simulations in a fluid damper containing high-viscosity silicone oils, modelled as single-mode linear Phan-Thien & Tanner [23] (PTT) viscoelastic liquids. The simulations are performed with an in-house Finite Volume solver. The PTT constitutive equation accounts for both shear-thinning and elasticity, and its parameters were selected so as to represent the rheological behaviour of high-viscosity silicone oils as recorded in the literature [10–12]). The viscoelastic simulations are complemented by simulations using the Carreau-Yasuda model which only accounts for shear-thinning but not elasticity, so as to investigate whether this inexpensive and easy to implement alternative suffices to produce realistic results, as has been assumed. The present results show that the PTT and CY models produce almost identical results at low oscillation frequencies, but at medium and high frequencies the PTT model does predict significant damper stiffness behaviour whereas the CY model does not. Furthermore, the PTT model, contrary to the CY, predicts significant variation of the fluid velocity along the piston-cylinder gap, i.e. that the flow in the gap is two-dimensional. This means that the theoretical approach based on the one-dimensional viscoelastic flow assumption, employed in [19, 14], is of limited accuracy. The study concludes with a brief investigation of flow with silicone oil of lower viscosity, to expose the main differences with the high-viscosity case.

Before ending this introductory section, it is worth mentioning that damper stiffness is observed experimentally also in other types of fluid damper, including magnetorheological (MR) [24, 3, 20, 8, 25] and extrusion dampers [26]. The experimental hysteresis loops obtained for these kinds of dampers are also qualitatively very similar to the present PTT results (but not the CY results), indicating that fluid elasticity is an important factor for these dampers as well. The fluids employed in MR and extrusion dampers additionally possess a yield stress, i.e. a limiting value of stress below which they do not flow but behave as solids; theoretical studies have thus far concentrated on the effect of yield stress, employing the Bingham [27, 28, 25, 22] or Herschel-Bulkley [20] constitutive models to describe the viscoplasticity of these fluids, but neglecting the elasticity. These models can explain the non-linear force-velocity relationship such as that expressed by Eq. (1), but not the damper stiffness (the spring-like property) such as expressed by Eqs. (2) and (3). The present results suggest that elasticity must be incorporated into these viscoplastic constitutive equations in order to obtain more realistic predictions.

2. Problem definition and governing equations

The geometry of the damper under consideration is shown in Fig. 1. It is of a simple and common design, consisting of a cylindrical piston of radius R_p and length L_p that reciprocates in a cylinder of radius R_c , forcing the fluid to flow through the annular gap of width $h = R_c - R_p$. The piston is fixed on a shaft of radius R_s that extends on both sides of the piston so that, as the shaft and piston oscillate, the fluid volume remains constant and compressibility effects are minimised; in fact in the present study the fluid is assumed to be incompressible in order to isolate the effects of the fluid viscoelasticity from other possible sources of damper stiffness such as fluid compressibility. The dimensions of the damper are listed in Table 1; they are in the range of sizes of silicone oil dampers used in experimental studies such as [14, 18]. In the literature the relative gap width h/R_c varies from small values for low viscosity oils (e.g. 0.022 for 1 Pa s oil in [14]) to large values for high viscosity oils (e.g. 0.412 for 630 Pa s oil in [16]), since the maximum damper force increases by increasing the fluid viscosity but decreases by increasing the gap width. In the present work the chosen model fluids have nominal viscosities of 100 and 500 Pa s and the relative gap width is set to $h/R_c = 0.120$.

This geometry is best fitted by a system of cylindrical polar coordinates (x, r, θ) (Fig. 1a), with $\underline{e}_x, \underline{e}_r, \underline{e}_\theta$ denoting the unit vectors along the coordinate directions. The flow is assumed to be axisymmetric, so that

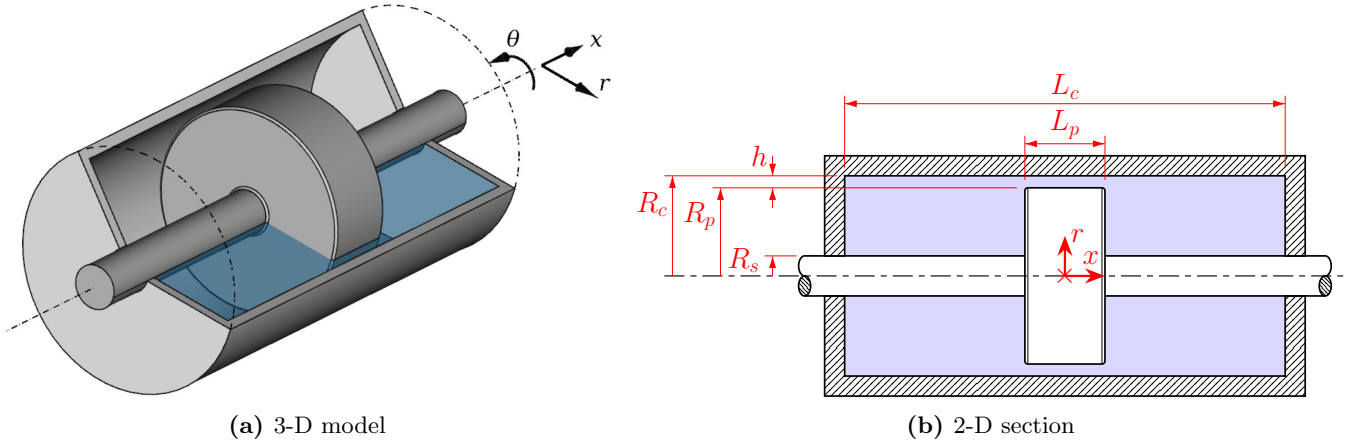


Figure 1: Layout of the damper. In (a) part of the cylinder is removed to reveal the shaft and piston. The flow is axisymmetric and can be solved on a single plane $\theta = 0$ (coloured in (a)).

the solution is independent of θ and the problem is reduced to two dimensions. The fluid velocity is denoted by \underline{u} , and its components are denoted by $u = \underline{u} \cdot \underline{e}_x$ (axial component) and $v = \underline{u} \cdot \underline{e}_r$ (radial component). The azimuthal velocity component, $\underline{u} \cdot \underline{e}_\theta$, is zero. The shaft is set to reciprocate along the axial direction such that the x -coordinate of the midpoint of the piston changes in time as

$$x_p(t) = \alpha \cos(\omega t) \quad (4)$$

where $x = 0$ is midway along the cylinder (point marked with \times in Fig. 1b), α is the amplitude of oscillation, and ω is the angular frequency related to the frequency f by $\omega = 2\pi f$. The period of oscillation is $T = 1/f = 2\pi/\omega$. For civil engineering applications the relevant frequencies are typically less than 4 Hz [1] although short, stiff structures may have natural frequencies of the order of 10 Hz [19]; in other applications, higher frequencies may be relevant. In the present work, simulations were performed for frequencies of $f = 0.5, 2, 8$ and 32 Hz, while the amplitude of oscillation was held fixed at $\alpha = 12$ mm. At the start of the simulation, at time $t = 0$, the fluid is assumed to be at rest. Once the shaft starts to move, after a transient period the flow will reach a periodic state where the flow field at time t will be identical to that at time $t - T$. In the present work we are interested in this periodic state, and due to viscoelastic effects this is attained faster if the initial piston velocity is zero, hence the imposed motion (4) contains a cosine term rather than a sine term. This means that at $t = 0$ the piston is located at its extreme right position. The velocity of the shaft and piston, dx_p/dt , is therefore

$$u_p(t) = -\alpha\omega \sin(\omega t) = -U_p \sin(\omega t) \quad (5)$$

where $U_p = \omega\alpha$ is the maximum piston velocity.

The flow inside the damper is governed by the following equations that express the mass and momentum balance of the fluid, respectively, at a microscopic (but continuum) level:

$$\nabla \cdot \underline{u} = 0 \quad (6)$$

Table 1: Dimensions of the damper, in millimetres (see Fig. 1b).

Cylinder radius, R_c	25
Cylinder length, L_c	110
Piston radius, R_p	22
Piston length, L_p	20
Gap width, $h = R_c - R_p$	3
Shaft radius, R_s	5

$$\frac{\partial(\rho \underline{u})}{\partial t} + \nabla \cdot (\rho \underline{u} \underline{u}) = -\nabla p + \nabla \cdot \underline{\underline{\tau}} \quad (7)$$

where t is time, \underline{u} is the velocity vector, p is the pressure, ρ is the density (which is constant, set to 1000 kg/m³), and $\underline{\underline{\tau}}$ is the stress tensor. To simplify the analysis the flow will be assumed incompressible and isothermal¹. These equations must be complemented by a constitutive equation that relates the stress tensor to the kinematics of the flow. The simplest such equation is the Newtonian one, $\underline{\underline{\tau}} = \eta \underline{\underline{\dot{\gamma}}}$, where η is the fluid viscosity and $\underline{\underline{\dot{\gamma}}} \equiv \nabla \underline{u} + (\nabla \underline{u})^T$ (T denoting the transpose) is the rate-of-strain tensor. However, this does not accurately describe the behaviour of polymeric liquids for all flow conditions. Such liquids consist of long molecular chains that interact with each other in a complex manner that typically results in a shear-thinning behaviour, i.e. the viscosity drops as the shear rate increases. This can be seen clearly in Fig. 2 where the symbols denote viscosity measurements at different shear rates in steady shear experiments, reported in [10, 12], for two different silicone oils with respective zero-shear viscosities of 90 and 525 Pa.s. Steady shear experiments [32] are typically performed in capillary or rotational rheometers where a velocity $\underline{u} \equiv (u_1, u_2, u_3) = (\dot{\gamma}_{12} x_2, 0, 0)$ is imposed on the fluid (as in Couette flow between parallel plates), $\dot{\gamma}_{12}$ being the only non-zero component of $\underline{\underline{\dot{\gamma}}}$, and the τ_{12} component of the stress tensor $\underline{\underline{\tau}}$ is measured; the viscosity is then defined as $\eta(\dot{\gamma}_{12}) \equiv \tau_{12}/\dot{\gamma}_{12}$. A simple and popular way to construct a shear-thinning constitutive equation is then to generalise the Newtonian one by allowing η to vary, $\underline{\underline{\tau}} = \eta(\dot{\gamma}) \underline{\underline{\dot{\gamma}}}$ where $\dot{\gamma} \equiv (\frac{1}{2} \underline{\underline{\dot{\gamma}}} : \underline{\underline{\dot{\gamma}}})^{1/2}$ is the magnitude of $\underline{\underline{\dot{\gamma}}}$ and the function $\eta(\dot{\gamma})$ is fitted to steady shear data such as those plotted in Fig. 2.

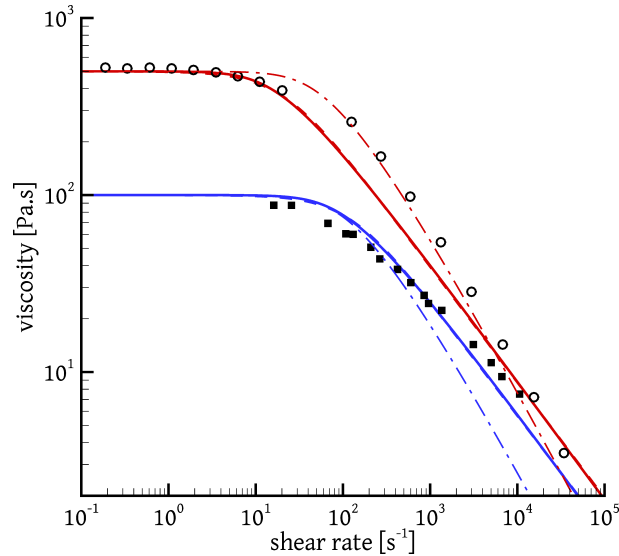


Figure 2: Variation of steady shear viscosity with shear rate, as measured for two different silicone oils (symbols) and predicted by constitutive models (lines). Experimental data are from [10] (■) and [12] (○). The continuous lines correspond to the linear PTT fluids IPTT-100 (blue) and IPTT-500 (red) of Table 2. Dashed lines correspond to the Carreau-Yasuda fluids CY-100 (blue) and CY-500 (red) of Table 2, but are nearly indistinguishable from the IPTT-100 and IPTT-500 lines. Dash-dot lines correspond to exponential PTT fluids with parameters $\{\eta = 100 \text{ Pa.s}, \lambda = 0.01 \text{ s}, \epsilon = 0.25\}$ (blue) and $\{\eta = 500 \text{ Pa.s}, \lambda = 0.06 \text{ s}, \epsilon = 0.025\}$ (red).

Figure 2 shows that the viscosity of silicone oil is nearly constant up to a critical shear rate beyond which it drops continually. A generalised Newtonian model capable of describing this kind of behaviour is

¹The temperature rise of the fluid due to viscous dissipation can be important and deserves a separate study. It is investigated theoretically in [29, 30] and experimentally in [13]. In [13], experiments performed with a damper of much larger size than the present model, showed that if the amplitude of oscillation is significantly greater than the piston diameter then the oil temperature in the neighbourhood of the piston can rise by 50 or more degrees Celsius during 6 oscillation cycles (the temperature rise is smaller farther away from the piston), which leads to a 10% drop in the maximum damper force during the same period. A force drop is expected, because such a temperature rise would reduce the oil viscosity to half its room temperature value [10, 31]. However, other experiments (again in [13]) with a smaller damper showed negligible effect of the temperature rise on the force magnitude, so this issue requires further investigation.

Table 2: Model fluids used in the simulations. In every case the density is $\rho = 1000 \text{ kg/m}^3$.

N-100:	Newtonian fluid of viscosity $\eta = 100 \text{ Pa s}$
IPTT-100	Eq. (9): $\eta_0 = 100 \text{ Pa s}$, $\lambda = 0.01 \text{ s}$, $\epsilon = 0.25$
CY-100	Eq. (8): $\eta_0 = 100 \text{ Pa s}$, $\dot{\gamma}_0 = 119 \text{ s}^{-1}$, $n = 0.353$, $m = 1.433$
IPTT-500	Eq. (9): $\eta_0 = 500 \text{ Pa s}$, $\lambda = 0.06 \text{ s}$, $\epsilon = 0.25$
CY-500	Eq. (8): $\eta_0 = 500 \text{ Pa s}$, $\dot{\gamma}_0 = 20.7 \text{ s}^{-1}$, $n = 0.346$, $m = 1.381$

the Carreau-Yasuda model [17], with four parameters² (η_0 , $\dot{\gamma}_0$, n , m):

$$\eta(\dot{\gamma}) = \eta_0 \left[1 + \left(\frac{\dot{\gamma}}{\dot{\gamma}_0} \right)^m \right]^{\frac{n-1}{m}} \quad (8)$$

At low shear rates ($\dot{\gamma} \ll \dot{\gamma}_0$) the model predicts Newtonian behaviour with viscosity $\eta = \eta_0$ while at high shear rates ($\dot{\gamma} \gg \dot{\gamma}_0$) the model predicts Power-Law behaviour $\eta = k\dot{\gamma}^{n-1}$ with shear-thinning index n and consistency index $k = \eta_0/\dot{\gamma}_0^{n-1}$; the exponent m determines how rapid the transition is from Newtonian to Power-Law behaviour as $\dot{\gamma}$ increases. As mentioned in Section 1, this model has been used to approximate the behaviour of damper fluids in the literature.

On the other hand, generalised Newtonian models do not account for fluid elasticity, which can affect the behaviour of the fluid in substantial ways. A popular viscoelastic model capable of describing the rheology of shear-thinning polymeric liquids is the Phan-Thien & Tanner (PTT) model [23, 33]; it has been used successfully to simulate several important processes of scientific and industrial interest (e.g. [34–38]). The simplified linear version of this model [23] can be expressed as

$$\underbrace{\left(1 + \frac{\lambda\epsilon}{\eta_0} \text{tr}(\underline{\underline{\tau}}) \right)}_{Y(\text{tr}(\underline{\underline{\tau}}))} \underline{\underline{\tau}} + \lambda \underline{\underline{\tau}}^\nabla = \eta_0 \dot{\underline{\underline{\tau}}} \quad (9)$$

where $\text{tr}(\underline{\underline{\tau}}) = \sum_i \tau_{ii}$ is the trace of the stress tensor, λ and η_0 are the fluid relaxation time and viscosity, respectively, and the triangle denotes the upper-convected derivative

$$\underline{\underline{\tau}}^\nabla \equiv \frac{\partial \underline{\underline{\tau}}}{\partial t} + \underline{u} \cdot \nabla \underline{\underline{\tau}} - ((\nabla \underline{u})^T \cdot \underline{\underline{\tau}} + \underline{\underline{\tau}} \cdot \nabla \underline{u}) \quad (10)$$

The PTT model (9) uses also a non-negative dimensionless parameter ϵ which is related to shear-thinning. A feel for the physical significance of the model can be obtained by noting that for $\epsilon = 0$, and viewing the upper convected derivative as a form of time derivative, the PTT model is analogous to the macroscopic Maxwell model (3) albeit applied to a microscopic fluid element³ instead of to the whole damper. In fact, for $\epsilon = 0$ the model (9) is called the Upper Convected Maxwell (UCM) model. For $\epsilon > 0$ the function $Y(\text{tr}(\underline{\underline{\tau}}))$ causes shear-thinning. This can be seen in Fig. 2 where the shear-thinning behaviour of the two linear PTT model fluids of Table 2 in steady shear flow is plotted (the solution of eq. (9) for steady shear flow can be found in [39]; see also Appendix A).

There is another version of the PTT model commonly in use, the exponential version [33], which differs from Eq. (9) in the definition of the function $Y(\text{tr}(\underline{\underline{\tau}})) = \exp((\lambda\epsilon/\eta) \text{tr}(\underline{\underline{\tau}}))$. The behaviour of a couple of such fluids is also plotted in Fig. 2 with dash-dot lines (see Appendix A for calculation details). It was noticed that for viscosities around 100 Pa s the exponential model predicts excessive shear thinning whereas

²The full Carreau-Yasuda model includes a fifth parameter, the viscosity limit η_∞ as $\dot{\gamma} \rightarrow \infty$. The experimental data for silicone oil [10, 12] such as those plotted in Fig. 2 do not reveal a non-zero such limit; therefore, we set $\eta_\infty = 0$, in which case the Carreau-Yasuda model reduces to Eq. (8).

³The ‘‘microscopic’’ fluid element is still much larger than the molecular dimensions so that the fluid can be regarded as a continuum.

the linear PTT model was closer to the experimentally observed behaviour of silicone oil. For viscosities around 500 Pa s the experimentally observed shear thinning is between that predicted by the two models. In the present work it was decided to use the linear PTT model, and in particular the fluids IPTT-100 and IPTT-500 of Table 2. The experimental data of the 90 Pa s and 525 Pa s silicone oils plotted in Fig. 2 were used as guides in selecting the PTT parameters, although a precise fitting to the data was not performed and the parameters were given nice, rounded values. In particular, as shown in Appendix A, the PTT parameter η_0 is equal to the viscosity at $\dot{\gamma} \rightarrow 0$ and values of $\eta_0 = 100$ Pa s and 500 Pa s were selected. On the other hand, as also shown in Appendix A, the data of Fig. 2 are not sufficient for obtaining realistic values for λ and ϵ individually because the curves of all PTT fluids for which the product $\epsilon\lambda^2$ is the same coincide. Therefore, the value of one of these parameters must come from another type of rheological experiment. The PTT parameter λ is intended to represent the fluid relaxation time, i.e. the time needed for stresses in the fluid to relax after the imposed shear rate is removed ($\dot{\gamma} = 0$). Longin et al. [11] provide experimental measurements of the storage and loss moduli of a 100 Pa s silicone oil, from which they derive a discrete spectrum of $N = 10$ relaxation moduli g_i , $i = 1, \dots, 10$, and associated relaxation times λ_i . From these we calculated the viscosity-averaged relaxation time as

$$\lambda = \frac{\sum_{i=1}^N g_i \lambda_i^2}{\sum_{i=1}^N g_i \lambda_i} \quad (11)$$

which gives a value of $\lambda = 0.01$ s. Assigning this value to λ for the IPTT-100 fluid, the value $\epsilon = 0.25$ was then chosen in order to obtain a nice viscosity versus shear rate curve compared to the data for a 90 Pa s silicone oil given in [10] (Fig. 2). A similar procedure was followed for the IPTT-500 fluid, using data from [12].

Flow simulations with a viscoelastic constitutive equation such as (9) are much more expensive than those with a generalised Newtonian constitutive equation such as (8) because in the latter the stress tensor is given by explicit expressions whereas in the former it has to be obtained through the solution of a partial differential equation for each relevant stress component. Thus it is tempting to assume that elasticity is not important and treat the flow as generalised Newtonian, accounting only for shear-thinning. To investigate how realistic such an assumption is for the present flow, we performed simulations also with the Carreau-Yasuda CY-100 and CY-500 fluids defined in Table 2, whose parameters were chosen such that they match the IPTT-100 and IPTT-500 fluids, respectively, in the plot of Fig. 2. This was achieved by fixing η_0 to 100 (for CY-100) and 500 (for CY-500) Pa s and selecting the rest of the parameters, $\dot{\gamma}_0$, m , n , such that they minimise the functional

$$\int_{\dot{\gamma}_1}^{\dot{\gamma}_2} [\ln(\eta_{\text{CY}}(\dot{\gamma}, \dot{\gamma}_0, m, n)) - \ln(\eta_{\text{PTT}}(\dot{\gamma}))]^2 d(\ln \dot{\gamma})$$

where $\dot{\gamma}_1 = 1$ (CY-100) or 0.1 (CY-500) and $\dot{\gamma}_2 = 10^5 \text{ s}^{-1}$ are the lower and upper limits of the shear-rate range of Fig. 2, η_{CY} is the Carreau-Yasuda viscosity function (8), and η_{PTT} is the steady shear viscosity of the linear PTT fluids plotted in Fig. 2. The resulting η_{CY} functions are plotted in dashed lines in Fig. 2 but are not discernible because they nearly coincide with the linear PTT viscosities. A few Newtonian simulations were also performed.

To some degree, whether inertia, shear-thinning, and elasticity of the fluid are important for this particular flow can be assessed a priori. This depends on the fluid properties, damper geometry, and operating conditions, and is expressed in terms of dimensionless numbers. Whether shear-thinning is important or not depends on the shear rates encountered. The highest shear rates will occur at the critical region of the gap between the piston and cylinder, when the piston velocity is maximum, i.e. when $|u_p| = U_p = \omega\alpha$ (Eq. (5)) at $t = T/4, 3T/4$, etc. At these times, the mean fluid velocity at the gap U_f can be found from the fact that the rate of fluid volume pushed towards one side by the piston, $U_p(\pi R_p^2 - \pi R_s^2)$, must equal the rate of fluid volume crossing the gap towards the other side, $U_f(\pi R_c^2 - \pi R_p^2)$, as follows from mass conservation and incompressibility. Therefore, $U_f = U_p(R_p^2 - R_s^2)/(R_c^2 - R_p^2)$. Assuming that the fluid velocity roughly varies from U_p at the piston surface to $-U_f$ at half-way between the piston and cylinder, a characteristic shear rate can be defined as $\dot{\gamma}_c \equiv U/(h/2)$ where $U = U_p + U_f$ is the relative velocity between the fluid and the piston. Table 3 lists the values of $\dot{\gamma}_c$ for the selected frequencies; from Eq. (8) or Fig. 2 we can deduce the viscosity that corresponds to each $\dot{\gamma}_c$, and compare it to the nominal η_0 . Table 3 also lists the ratios

Table 3: Operating conditions for which simulations were performed, and associated dimensionless numbers. The oscillation amplitude is $\alpha = 12$ mm in every case.

	100 Pa.s				500 Pa.s	
f [Hz]	0.5	2	8	32	0.5	2
U_p [m/s]	0.038	0.151	0.603	2.413	0.038	0.151
U [m/s]	0.16	0.64	2.57	10.27	0.16	0.64
$\dot{\gamma}_c$ [s^{-1}]	107	428	1711	6845	107	428
$\eta(\dot{\gamma}_c)/\eta_0$	0.759	0.399	0.178	0.078	0.315	0.137
Re	0.002	0.010	0.039	0.154	0.001	0.002
Re_c	0.003	0.024	0.216	1.984	0.002	0.014
Wi	1.07	4.28	17.1	68.5	6.42	25.7
De	0.005	0.02	0.08	0.32	0.03	0.12
Sr	214	214	214	214	214	214

$\eta(\dot{\gamma}_c)/\eta_0$, and from these values it is evident that shear-thinning is expected to play a very significant role, even at low frequencies.

To assess the importance of inertia and elasticity, it is expedient to express the governing equations in dimensionless form. To this end, we normalise lengths by half the gap width, $H \equiv h/2$, time by the period of oscillation T , velocities by $U = U_p + U_f$, and stresses and pressure by $\eta_0 U/H$. Whence substituting $x = \tilde{x}H$, $t = \tilde{t}T$, $\underline{u} = \tilde{u}U$ etc. Eqs. (7) and (9) – (10) can be expressed as

$$Re \left(\frac{1}{Sr} \frac{\partial \tilde{u}}{\partial \tilde{t}} + \tilde{\nabla} \cdot (\tilde{u}\tilde{u}) \right) = -\tilde{\nabla} \tilde{p} + \tilde{\nabla} \cdot \tilde{\underline{\underline{\tau}}} \quad (12)$$

$$(1 + \epsilon Wi \text{tr}(\tilde{\underline{\underline{\tau}}})) \tilde{\underline{\underline{\tau}}} + \left(De \frac{\partial \tilde{\underline{\underline{\tau}}}}{\partial \tilde{t}} + Wi \left(\tilde{u} \cdot \tilde{\nabla} \tilde{\underline{\underline{\tau}}} - (\tilde{\nabla} \tilde{u})^T \cdot \tilde{\underline{\underline{\tau}}} - \tilde{\underline{\underline{\tau}}} \cdot \tilde{\nabla} \tilde{u} \right) \right) = \tilde{\underline{\underline{\dot{\gamma}}}} \quad (13)$$

where $Re \equiv \rho UH/\eta_0$ is the Reynolds number, $Sr \equiv T/(H/U)$ is the Strouhal number, $Wi \equiv \lambda U/H$ is the Weissenberg number, $De \equiv \lambda/T (= Wi/Sr)$ is the Deborah number, and the tilde ($\tilde{\quad}$) denotes dimensionless quantities, with $\tilde{\underline{\underline{\dot{\gamma}}}} \equiv \dot{\gamma}/(U/H)$.

The Reynolds and Strouhal numbers appear in the convection terms of the momentum equation. For this particular problem, it follows from $T = 2\pi/\omega$ and $U = U_p + U_f = \alpha\omega(1 + (R_p^2 - R_s^2)/(R_c^2 - R_p^2))$ that $Sr = \tilde{\alpha} 2\pi(R_c^2 - R_s^2)/(R_c^2 - R_p^2)$ where $\tilde{\alpha} \equiv \alpha/H$ is the dimensionless oscillation amplitude. Thus, the inherent inversely proportional relationship between the velocity U and the period T removes the dependence of Sr on f and makes it a function of only the oscillation amplitude and the damper geometry, which are held constant in the present study. The Reynolds number is an indicator of the ratio of fluid inertia to viscous forces, and its values for each fluid / frequency combination are listed in Table 3. This definition of Reynolds number does not account for shear-thinning and overestimates the viscous forces, so the Table includes also a Reynolds number based on the viscosity at the characteristic shear rate, $Re_c \equiv \rho UH/\eta(\dot{\gamma}_c)$. The values of both Reynolds numbers can be seen to be small, making the left-hand side of the momentum equation (12) small compared to the two terms appearing in the right-hand side. Thus the role of fluid inertia is expected to be limited in the present flow; nevertheless, the inertia terms were retained in the equations solved and it will be seen in Sec. 4.3 that inertia does play a minor role for this flow, at high frequencies.

The Weissenberg number is an indicator of the ratio of elastic to viscous forces, while the Deborah number is the ratio of the fluid relaxation time to a time scale characterising the flow, which in our case is the oscillation period T [40]. Both numbers are indicative of the importance of elastic phenomena in the flow, and it may be seen that if they tend to zero then the constitutive equation (13) tends to the Newtonian constitutive equation. However, the values listed in Table 3 are not small, and suggest significant elastic effects.

Before ending this section, one more issue must be discussed. Calculation of the damper force is of crucial importance, and is performed by integrating the stress and pressure over the surface of the piston and the shaft. At the points where the moving shaft meets the stationary cylindrical casing the wall velocity varies discontinuously. If the fluid is Newtonian and the no-slip boundary condition is assumed then it can be shown [41] that the shear stress on the shaft varies as $(\delta x)^{-1}$, where δx is the distance from the singularity point. The force on the shaft is equal to the integral of the shear stress over the shaft surface, i.e. it is proportional to the integral of $(\delta x)^{-1}$ from $\delta x = 0$ to the length of the shaft, which is infinite. Clearly, an infinite force is not a realistic result. In our previous work [22] this hurdle was overcome by assuming a Navier slip boundary condition, which was shown to limit the force to finite values [42], and is a realistic assumption according to molecular simulation studies [43, 44] even for Newtonian flows. In non-Newtonian flows slip phenomena are much more pronounced [45–48]. To be consistent with our previous approach, in the present study we also employed Navier slip boundary conditions, in fact on all solid walls; thus, if \underline{u} and \underline{u}_w are the fluid and wall velocities at the boundary then

$$(\underline{u} - \underline{u}_w) \cdot \underline{s} = \beta(\underline{n} \cdot \underline{\tau}) \cdot \underline{s} \quad (14)$$

where \underline{n} is the unit vector normal to the wall and \underline{s} the unit vector tangential to the wall within the plane in which the equations are solved. The slip coefficient β is assigned here values of 5×10^{-7} m/Pa s (IPTT-100 and CY-100 fluids) and 10^{-6} m/Pa s (IPTT-500 and CY-500 fluids). These values are significantly lower than those used in our previous work [22]. A feel for the effect of slip in the critical region of the gap can be obtained as follows. Assume that the flow in that region is one-dimensional and the stress on the cylinder, $(\underline{n} \cdot \underline{\tau}) \cdot \underline{s} = \tau_{rx}$, is typically of order $\eta(\dot{\gamma}_c)U/H$ (Table 3) when the cylinder moves with maximum velocity. Then from Eq. (14) it follows that

$$u - u_w = \beta \eta(\dot{\gamma}_c) \frac{U}{H} \Rightarrow \frac{u - u_w}{U} = \frac{\beta \eta(\dot{\gamma}_c)}{H}$$

(the product $\beta\eta$ is called the *slip length*). The right-hand side has values ranging from 2.5% ($f = 0.5$ Hz) to 0.26% ($f = 32$ Hz) for the 100 Pa s fluids, and from 10.5% ($f = 0.5$ Hz) to 4.6% ($f = 2$ Hz) for the 500 Pa s fluids. Thus the slip velocity $u - u_w$ is small, but not negligible, compared to the velocity scale U and the flow is not much affected by the wall slip (this is confirmed by the velocity profiles shown in Fig. 18, to be discussed in Sec. 4.4). We note that the $(\delta x)^{-1}$ stress variation of Newtonian fluids is barely non-integrable; a variation $(\delta x)^{-a}$ would be integrable for any $a < 1$ and result in finite force. Therefore, it is reasonable to expect that for shear-thinning fluids whose viscosity tends to zero as the shear rate tends to infinity, such as those presently employed, the force would be finite even with the no-slip boundary condition. However, this issue was not investigated further.

3. Numerical method

The equations given in the previous Section were solved using a finite volume method, which was developed on the foundation of an existing method for generalised Newtonian and viscoplastic flows [49, 50, 22]. In the present Section the method will only be summarised, while the extensions pertaining to viscoelastic flow will be described in detail in a separate publication.

The $x - r$ plane was discretised by a series of block-structured grids of increasing fineness, a coarse one of which is shown in Figs. 3a and 3b. The grid changes dynamically in time in order to follow the motion of the piston: the cells surrounding the piston up to 2.5 mm on either side translate along with it without deforming, while the rest of the grid cells contract or expand accordingly (Figs. 3a, 3b). Since the solution of the set of discretised equations was accelerated using a multigrid algorithm, grids of varying fineness were created. Solutions were obtained on the three finest grids, the sizes of which are listed in Table 4. The same Table lists the number of cells in the radial direction between the piston and the cylinder, which are of equal radial width. Preliminary simulations suggested that using sharp piston corners does not create additional numerical difficulties, but to be on the safe side [51] it was decided to use rounded corners, of radius 0.75 mm, as shown in Fig. 3c. The blocks in contact with these corners were constructed using an elliptic grid generation technique [52, 53].

Concerning the discretisation of the momentum and continuity equations, we used the same method as in our previous work [22], which employs central differencing with least-squares gradients [54] in space and

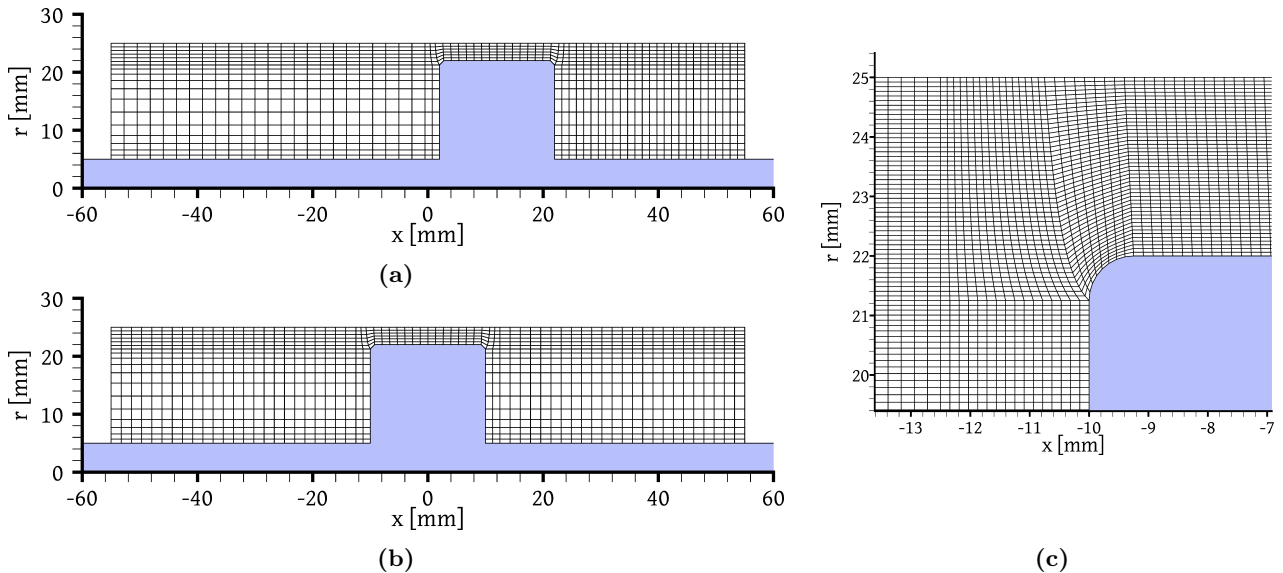


Figure 3: (a) View of a coarse grid at a time instance when the piston is at the extreme right position. (b) View at a time instance when the piston is at the middle position. (c) Close-up of grid 2 (Table 4) near a piston corner.

Table 4: Sizes of the grids used in the simulations.

Grid	total cells	cells across gap
1	16,512	24
2	66,048	48
3	264,192	96

a three time level implicit scheme in time, which are second-order accurate. A complication arises in the viscoelastic case because the viscous forces on the cell faces are not an explicit function of the velocity but are calculated by linear interpolation of the stresses at the cells on either side of the face, which are stored as separate variables. This results in a lack of second derivatives of velocity in the momentum equation (7) and leaves only the first derivatives of the convection terms, which makes the solution susceptible to spurious velocity oscillations, in exactly the same way that the appearance of only first derivatives of pressure in the same equation gives rise to the well-known problem of spurious pressure oscillations. In the present work, the pressure oscillations were suppressed by using a variant, proposed in [49], of the renowned “momentum interpolation” technique [55] while the velocity oscillations were suppressed in a similar manner, by devising a scheme for interpolation of the stresses at cell faces that is inspired from the one proposed in [56, 57] and re-introduces (discrete) second derivatives of velocity into the momentum equation. The details of this interpolation scheme, which follows the philosophy of our momentum interpolation scheme [49], will be given in a separate publication. The momentum convection terms were discretised with plain central differences; the aforementioned stress interpolation scheme proved effective in eliminating the velocity oscillations such that a high-resolution scheme (e.g. CUBISTA – see below) was not necessary for these terms.

The viscoelastic constitutive equations were discretised along similar lines as in [56, 58]. To reduce their stiffness, these equations were expressed in terms of the logarithm of the conformation tensor instead of the stress tensor itself, as suggested in [59, 21, 60]. The viscoelastic constitutive equation (9) contains no diffusion terms, and therefore again a spurious stress oscillation issue may arise; to avoid it, its convection terms were discretised with the CUBISTA high resolution scheme [61]. At domain boundaries, all of which are solid walls, the pressure and stresses were linearly extrapolated from the interior. The system of non-linear algebraic equations that arise from the finite volume discretisation was solved with an extended SIMPLE algorithm, each iteration of which includes the solution of one linear system per component of the log-conformation tensor. The SIMPLE solver was used as a smoother in a multigrid framework [50]. For

one of the test cases, the lPTT-500 fluid at the $f = 2$ frequency, the SIMPLE / multigrid solver exhibited convergence difficulties that were overcome by applying a vector extrapolation technique [62] where each vector contains the estimate of all log-conformation tensor components (rr , xx , rx , and $\theta\theta$) at all grid cells after a multigrid cycle.

The code was validated against available data on viscoelastic lid-driven cavity flows, which resemble the present flow configuration in that they are bounded all around by solid walls and the flow is induced by a moving wall. Comparison of results obtained with our code against results presented in the literature shows very good agreement. Indicative results concerning the location and strength of the main vortex are shown in Table 5. The model fluids include a Newtonian solvent contribution to the stress tensor: $\underline{\underline{\tau}} = \underline{\underline{\tau}}_p + \underline{\underline{\tau}}_s$ where the polymeric component $\underline{\underline{\tau}}_p$ is given by Eq. (9) and the solvent component by $\underline{\underline{\tau}}_s = \eta_s \dot{\underline{\underline{\gamma}}}$. Then the flow is determined by an additional dimensionless number, the viscosity ratio $B \equiv \eta_s / (\eta_s + \eta_p)$ where η_p is the viscosity of the polymeric component, denoted as η_0 in Eq. (9).

Table 5: \tilde{x} - and \tilde{y} - coordinates (first and second columns) of the centre of the main vortex for viscoelastic flow in a square cavity of side H , and associated value of the streamfunction there (third column). The top wall moves in the positive x -direction with variable velocity $u(x) = 16U(x/H)^2(1 - x/H)^2$ (for the $\epsilon = 0$ case), or with uniform velocity $u = U$ (for the $\epsilon = 0.25$ cases); The coordinates are normalised by the cavity side H and the streamfunction by UH . The Weissenberg and Reynolds numbers are defined as $Re \equiv \rho UH / (\eta_s + \eta_p)$ and $Wi \equiv \lambda U / H$, respectively.

$\epsilon = 0, Wi = 1, Re = 0, B = 0.5$			
Saramito [63]	0.429	0.818	-0.0619
Sousa et al. [64]	0.434	0.814	-0.0619
Present results	0.434	0.818	-0.0619
$\epsilon = 0.25, Wi = 4, Re = 1, B = 1/9$			
Dalal et al. [65]	0.429	0.812	-0.0694
Present results	0.430	0.813	-0.0693
$\epsilon = 0.25, Wi = 4, Re = 100, B = 1/9$			
Dalal et al. [65]	0.783	0.767	-0.0594
Present results	0.782	0.760	-0.0600

Each damper flow simulation had a total duration of six periods, of which the first two were calculated on grid 1, the following two on grid 2, and the last two on grid 3 (Table 4). To ensure that the last (sixth) period represents the periodic state, we compared force versus shaft displacement diagrams for periods 2, 4 and 6, with indicative results shown in Fig. 4. As can be seen from the figures, the force changes very little between periods 2, 4 and 6 which suggests that the periodic state is reached quickly, and also that grid convergence has been achieved on grid 3 (because periods 2, 4 and 6 are calculated on different grids). We note that as viscoelasticity (Wi) increases the force difference between different grids grows, which shows that increasing viscoelasticity necessitates the use of finer grids to maintain a given level of accuracy. The results suggest that the error on the finest grid is in each case less than 1 %. The force calculated on grid 2 for the lPTT-100 fluid at $f = 32$ Hz (Fig. 4f) has a component that oscillates in time (which is responsible for the relatively large zero-displacement force difference of 2.63% between grids 2 and 3) but this vanishes on the finest grid.

The time step used in the simulations was $\Delta t = T/4000$ for the CY and Newtonian fluids and $\Delta t = T/8000$ for the l-PTT fluids. Since the Reynolds numbers are small, the inertial terms in the momentum Eq. (12), which include the temporal term, are not very significant and thus for the Newtonian and CY simulations the flow is quasi-steady [22] (or nearly so) and the choice of time step is not crucial (the chosen $\Delta t = T/4000$ is most probably unnecessarily small). On the other hand, for the viscoelastic simulations a temporal term appears also in the constitutive Eq. (13) which, according to the values of Wi and De listed in Table 3, may be significant; hence the small chosen time step $\Delta t = T/8000$ for the viscoelastic simulations.

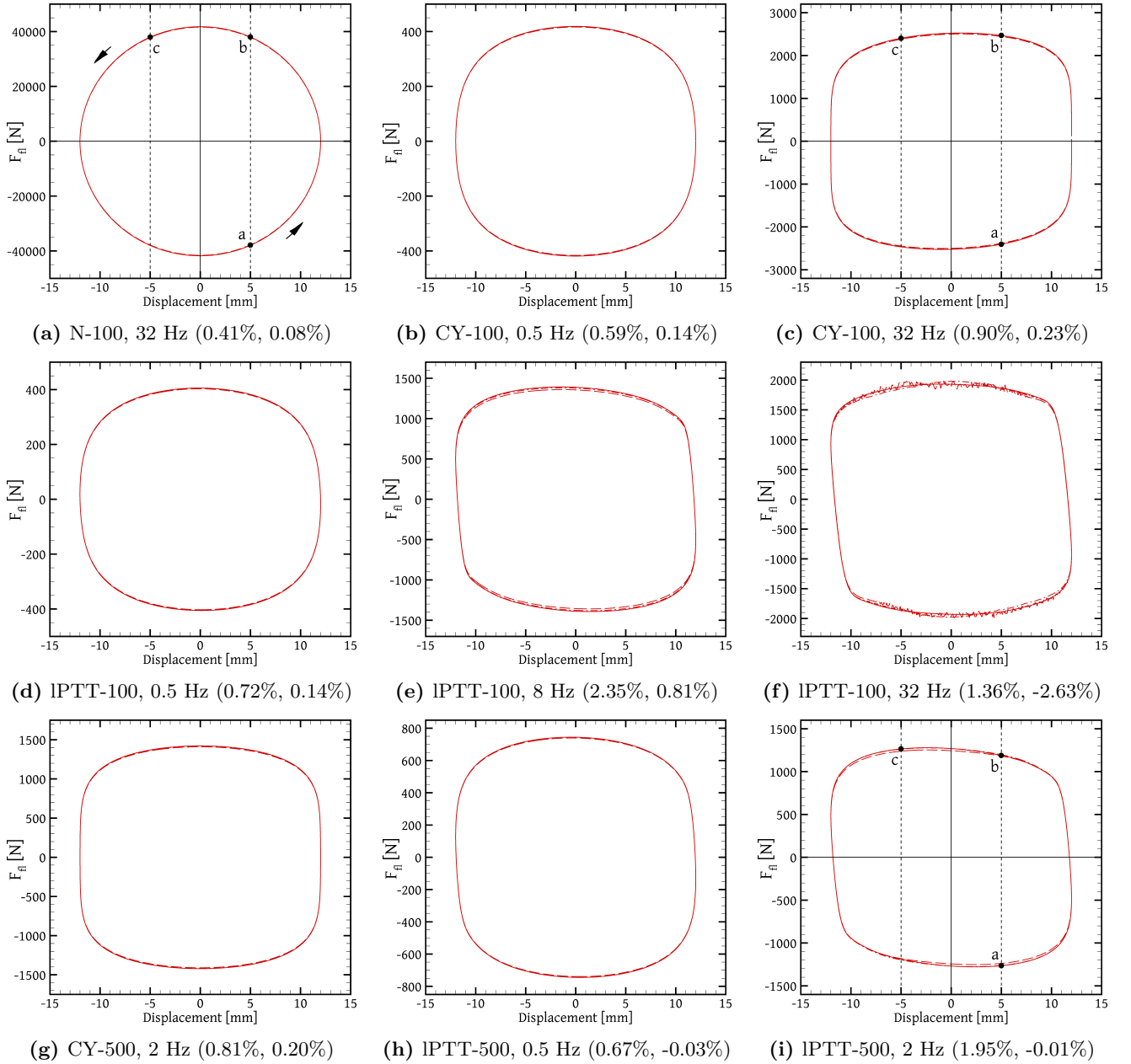


Figure 4: Diagrams of the force F_{fl} , Eq. (17), versus displacement of the piston midpoint compared to the $x = 0$ position, for various fluids and frequencies. Dashed lines: period 2, calculated on grid 1; dash-dot lines: period 4, calculated on grid 2; continuous lines: period 6, calculated on grid 3. The numbers in parentheses are the percentage difference in force at zero displacement between grid 3 and either grid 1 (first number) or grid 2 (second number). The loops are traversed in the anticlockwise sense as time progresses.

This is 20 times smaller than that used in our previous study [22], and was found to offer adequate accuracy by tests where the time steps used on the coarse grids 2 and 1 were, respectively, two ($\Delta t = T/4000$) and four ($\Delta t = T/2000$) times larger than this value, which was used on grid 3. For example, this procedure for the IPTT-100, $f = 8$ Hz case yielded force differences at zero displacement of 1.85% and 0.68% between grids 3 and 1, and 3 and 2, respectively. These differences are even smaller than those reported in Fig. 4e, which suggests that the spatial and temporal discretisation contributions to the discretisation error are of opposite sign. The present choice of time step, which is coupled to the oscillation period, leads to variable resolutions of the relaxation time depending on the oscillation frequency, namely to ratios $\lambda/\Delta t$ of 40, 160, 640 and 2560 at $f = 0.5, 2, 8$ and 32 Hz, respectively, for the IPTT-100 fluid and of 240 and 960 at $f = 0.5$ and 2 Hz, respectively, for the IPTT-500 fluid. At low frequencies this ratio is small, but the Wi and De numbers are small as well (Table 3) and the importance of viscoelasticity diminishes, as the results of Sec. 4 will confirm, so that a high resolution of the viscoelastic phenomena is not necessary in order to

accurately simulate the flow. Finally, we note that the Courant-Friedrichs-Lewy number (CFL) on the finest grid can be approximated as $U\Delta t/(h/96)$ where $h/96$ is the grid spacing across the gap, which gives CFL values of 2.56 and 1.28 for the CY and l-PTT fluids, respectively (independent of the frequency f). The CFL number is used in explicit temporal discretisation schemes to control their stability; while the present method is implicit and a CFL < 1 is not a prerequisite for stability, usually a CFL number smaller than unity indicates adequate temporal resolution in relation to the spatial resolution. In [66], where the same temporal discretisation scheme was used, good accuracy was reported with CFL numbers as high as 3–6.

4. Results

In an experimental study, the damper under investigation would be subjected to a predetermined displacement history, and the required force that causes this displacement would be recorded using a load cell. This applied force, F_{ap} , causes the acceleration of the shaft-piston assemblage, and is counteracted by the force F_{fl} exerted by the fluid on the shaft-piston and by the friction force F_{fr} at the damper bearings and seals. Therefore, Newton's second law can be expressed as

$$F_{ap} + F_{fl} + F_{fr} = M_p a_p \quad (15)$$

where M_p is the mass of the shaft-piston assemblage and a_p is its acceleration. The latter is obtained by differentiating Eq. (5):

$$a_p(t) = -\alpha\omega^2 \cos(\omega t) = -A_p \cos(\omega t) \quad (16)$$

where $A_p = \alpha\omega^2$ is the maximum acceleration, occurring when the piston reaches its extreme positions.

The present numerical simulations allow prediction of the reaction force exerted by the fluid on the piston and shaft, by integrating the stress and pressure over the piston surface and on the part of the shaft's surface that is immersed in the fluid:

$$F_{fl} = \iint_S (-p\underline{n} + \underline{n} \cdot \underline{\tau}) \cdot \underline{e}_x \, ds \quad (17)$$

where S is the shaft-piston surface, ds is an infinitesimal element of that surface, and \underline{n} is the unit vector normal to that surface at each point, directed towards the fluid. It is mostly on this force that the present study focuses. If the friction force F_{fr} and the piston inertia term $M_p a_p$ are assumed negligible, then Eq. (15) reduces to

$$F_{ap} \approx -F_{fl} \quad (18)$$

Therefore, the plots of F_{fl} presented in this study, such as in Fig. 4, resemble mirror images of experimentally derived plots of F_{ap} provided in the literature. However, in Section 4.5 plots of F_{ap} itself will also be presented, derived from Eq. (15) with the shaft inertia included but F_{fr} neglected.

Customarily, the damper behaviour is explored through the examination of plots of force versus piston displacement and piston velocity, which are easily obtainable in experimental studies. The present study includes such plots but is not restricted to these. One of the advantages of numerical simulation is that it provides estimates of all the flow variables at every point in the domain and at every time instance, thus providing a complete picture of the flow. This is exploited in order to go beyond the force-displacement/velocity plots and obtain additional insight. Since we are interested in the periodic state, the plots presented in this study correspond to the sixth oscillation period simulated ($t \in [5T, 6T]$), unless otherwise stated, in order to avoid any initial transient phenomena (although it was noticed that the periodic state is attained fairly quickly, with transient phenomena not persisting beyond the first period).

The area enclosed by the loops of force-displacement plots is equal to the energy absorbed by the damper in a single cycle and converted into heat by viscous action in the fluid⁴. A look at Fig. 4 shows that the

⁴The instantaneous energy balance for the damper fluid includes the rate of work of the force F_{fl} , the rate of viscous dissipation of energy into heat, and the rate of change of energy stored in the fluid in the form of elastic energy. However, considering a full period of oscillation, if the flow has reached the periodic state, the stored elastic energy at time t is exactly equal to that at time $t + T$. Therefore, the work of F_{fl} during a complete cycle is equal to the amount of energy dissipated to heat by viscous action during the same period.

elliptical shape of the Newtonian loop 4a is distorted towards a rectangular shape when the fluid is non-Newtonian, stretched in a direction that forms either a positive (counterclockwise) angle, for CY fluids (e.g. Fig. 4c), or a negative (clockwise) angle, for PTT fluids (e.g. Fig. 4i), compared to the horizontal axis. The non-Newtonian characteristics become more prominent as the frequency and/or zero-shear viscosity (η_0) increase. In force-displacement diagrams, this tilting of the loop at an oblique angle is a definite sign of *hysteresis*, i.e. of dependence of the current state of the flow on its history.

When the Reynolds number in Eq. (12), and, for PTT fluids, the Wi and De numbers in Eq. (13), are very small then the corresponding terms become negligible and the governing equations become elliptic and quasi-steady state, so that the flow is not affected by its own history but is determined solely by the instantaneous boundary conditions. In this case, symmetry between two instantaneous damper states, such as any pair of the states (a), (b) and (c) depicted in Fig. 5, results in identical force magnitudes. Such is the flow of the N-100 fluid even at the highest frequency of 32 Hz (Fig. 4a) because of the very large viscosity of the fluid. In Fig. 4a the three states (a), (b) and (c) are marked (the displacement d of Fig. 5 is arbitrarily set equal to 5 mm in Fig. 4) and it can be seen that $|F_{fl}(a)| = |F_{fl}(b)| = |F_{fl}(c)|$. The N-100 loop is symmetric with respect to both the force = 0 and displacement = 0 axes.

On the other hand, for the CY and PTT fluids as the frequency increases the transient terms in Eqs. (12) and (13) become more important and the flow history comes into play. Now, although damper states (a) and (b) are symmetric, they have different histories and therefore $|F_{fl}(a)| \neq |F_{fl}(b)|$ in both Fig. 4c and Fig. 4i. However, states (a) and (c) are not only symmetric, but the histories of the flows leading up to these states are also symmetric; therefore, $|F_{fl}(a)| = |F_{fl}(c)|$. Half a period suffices to describe the whole loop (the flow fields at times t and $t + T/2$ are symmetric).

It is customary to also plot the force versus the piston velocity, as in Fig. 6. We shall use the normalised velocity u_p/U_p (Eq. (5)) for such plots, which allows to plot the loops of different frequencies on the same diagram (the maximum piston velocities U_p for each frequency are listed in Table 3). The effects of the non-Newtonian character of the fluids are even more pronounced on force-velocity plots, especially at higher frequencies (Fig. 6b) whereas at low frequencies the behaviour deviates mildly from the Newtonian one (Fig. 6a). In force-velocity plots hysteresis is manifest in the plot having the form of a loop rather than of a single curve. This means that, by drawing a vertical line on the graph, for a given piston velocity there are two different values of force: one value is exhibited when the piston is accelerating, and a different value when it is decelerating. This can be observed in Fig. 6b where $F_{fl}(b) \neq F_{fl}(c)$ for both the CY and PTT fluids, whereas $F_{fl}(b) = F_{fl}(c)$ for the Newtonian fluid (the states (a), (b), (c) have been arbitrarily set to correspond to a normalised velocity of ± 0.3).

The force-displacement and force-velocity plots are very reminiscent of the Lissajous-Bowditch plots obtained in Large Amplitude Oscillatory Shear (LAOS) experiments [67], i.e. plots of shear stress versus strain or rate-of-strain, respectively, which are used for the characterisation of soft materials and complex fluids. A brief description of LAOS is given in Appendix B. This similarity allows us to borrow some tools from LAOS theory in the following sections. However, it must be noted that there are also significant differences between LAOS and the present flow: whereas in LAOS all the material undergoes the same deformation simultaneously in a Couette-type flow, the damper flow is two-dimensional and mostly pressure driven, with the stress and deformation rate varying along both the gap length and width, while each fluid particle remains in the critical gap region for only a limited amount of time during each period, provided that the oscillation amplitude is not very small.

The precise shapes of the force-displacement and force-velocity plots will be examined in greater detail in the sections that follow, but first a general description of the flow field inside the damper will be given.

4.1. General description of the flow field

Before examining the force F_{fl} it is worthwhile to examine some snapshots of the whole flow field in Fig. 7. All snapshots correspond to a time instance when the piston moves towards the right with maximum velocity. The general picture that these snapshots present is that the rightward piston motion forces oil to flow from the right damper compartment to the left compartment through the narrow annular gap, which gives rise to a sharp pressure gradient along the gap length in order to overcome the stresses that resist this fluid motion. The resulting large pressure difference between the left and right sides of the piston causes a pressure force that opposes its motion. The latter is also opposed by the stresses in the gap region, but

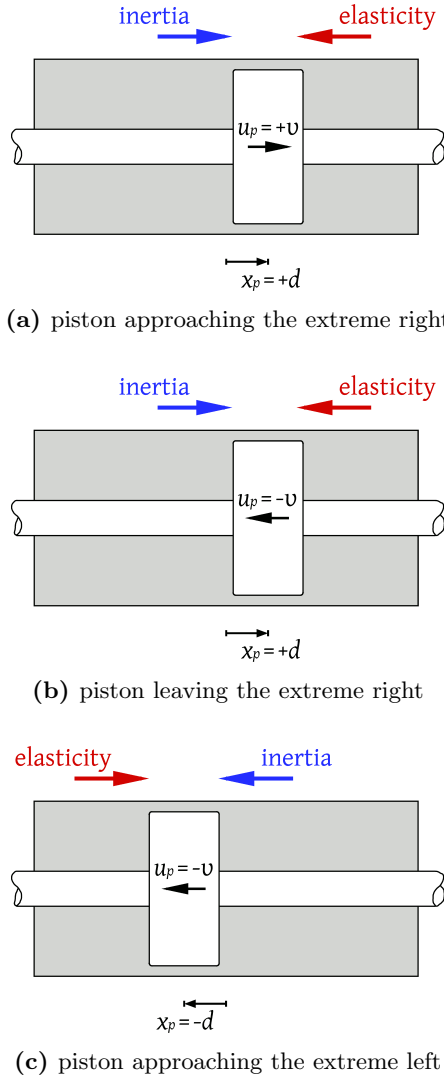


Figure 5: The damper at three different “symmetric” time instances: At (a) the piston is displaced towards the right and is moving towards the right. Later, at (b), the piston has returned to the same position ($x_p(b) = x_p(a)$) but is moving towards the left ($u_p(b) = -u_p(a)$). Later still, at (c), the piston has moved to the opposite side ($x_p(c) = -x_p(b)$) and is moving towards the left ($u_p(c) = u_p(b)$). The directions of the inertial and elastic components of the fluid force on the piston and shaft are shown in each case.

the pressure contribution to the total force F_{fl} is much larger for this damper configuration: as shown in Fig. 8, the pressure force is nearly ten times larger than the force due to shear stresses. Figure 8 also shows that F_{fl} arises mostly on the piston surface, while the contribution of the shaft surface to the total force is negligible.

The instantaneous streamlines shown in Fig. 7 are drawn equispaced along the vertical piston walls in the r -direction. The flow rate between any pair of streamlines can be calculated from the piston velocity and the area between the points where these streamlines touch the vertical piston walls. Because the domain is axisymmetric, this area, and therefore also the flow rate, between a pair of successive streamlines that are close to the shaft (small r coordinate) is smaller than that between a pair of successive streamlines that lie closer to the outer cylinder (large r coordinate). Therefore, it is evident from all snapshots of Fig. 7 that the flow is mostly restricted to the immediate neighbourhood of the piston. Fluid that gets pushed out of the way in front of the piston quickly rises, passes through the gap, and travels to the region immediately behind the piston. Fluid that is located farther away remains relatively at rest.

In Fig. 7, the left column of snapshots corresponds to the Carreau-Yasuda fluids, while the right column contains the corresponding snapshots predicted by the l-PTT fluids. The Carreau-Yasuda model predicts a smooth, symmetric flow field in every case examined. This is due to the fact that the inertial character of this flow is weak; it is not hard to show that for a symmetric domain, such as the present one when the

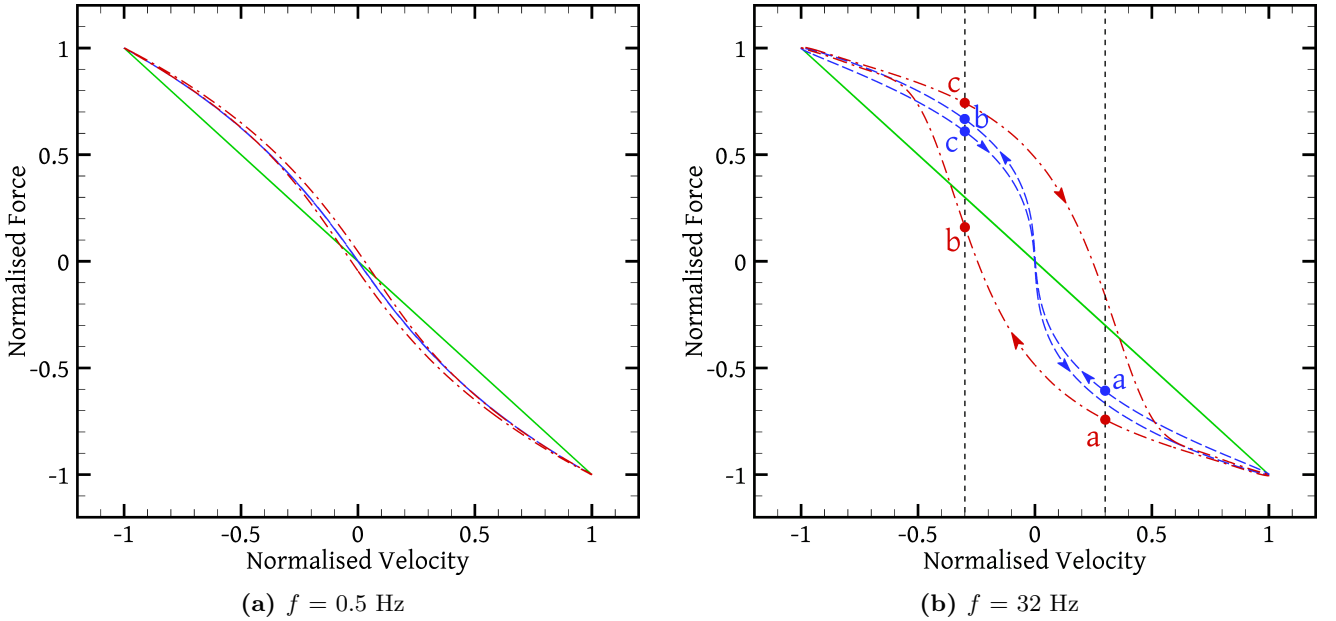


Figure 6: Force F_{fl} normalised by its maximum value, against piston velocity normalised by its maximum value (u_p/U_p , Eq. (5)), for the N-100 (solid green line), CY-100 (dashed blue line) and IPTT-100 (dash-dot red line) fluids at $f = 0.5$ Hz (left) and 32 Hz (right). The CY-100 loops are traversed in the counterclockwise sense whereas the IPTT-100 loops in the clockwise sense.

piston lies halfway along the cylinder, the momentum equation (12) in the limit of $Re \rightarrow 0$ (creeping flow), with a generalised Newtonian constitutive equation $\underline{\underline{\tau}} = \eta(\dot{\underline{\underline{\gamma}}})\dot{\underline{\underline{\gamma}}}$, admits symmetric solutions. The vanishing of the time derivative in the momentum equation (12) as $Re \rightarrow 0$ also makes the flow field quasi-steady (not dependent on the previous flow history but only on the instantaneous boundary conditions) and therefore the choice of time step in the numerical solution procedure has a small impact on the accuracy.

The predictions of the IPTT-100 fluid at the lowest frequency of $f = 0.5$ Hz (Fig. 7b) are nearly identical to those of the CY-100 fluid (Fig. 7a). This suggests that at low frequencies the Carreau-Yasuda generalised Newtonian model suffices to describe the behaviour of silicone oil because the Weissenberg number is low and elastic effects are not important. However, at higher Weissenberg numbers, which result from higher frequency (Fig. 7d) or fluid elasticity (Fig. 7f), there are major deviations of the viscoelastic predictions from those of the generalised Newtonian model. The viscoelastic flow is unsymmetric and less smooth, and these features become more pronounced as the Weissenberg number increases (compare Fig. 7d with $Wi \approx 70$ against Fig. 7f with $Wi \approx 25$). Now the flow cannot be characterised as quasi-steady, despite the low Reynolds number that suppresses the inertial terms in the momentum equation (12), because transient effects are important in the constitutive equation (13) and govern the evolution of the stresses. In Figs. 7d and 7f one can notice that the flow in the upstream chamber (on the right of the piston) resembles more the corresponding generalised Newtonian flow than that in the downstream (left) chamber. This can be attributed to the fact that the fluid upstream of the piston has not undergone significant deformations recently and the stresses have had some time to relax; therefore, the state of the fluid is somewhat similar to that of the corresponding Carreau-Yasuda fluid, as can be more clearly seen by comparing Figs. 7f and 7e. Once the fluid has been pushed through the narrow gap, the large stresses developed there relax gradually in the PTT case but immediately in the CY case. Therefore, the PTT and CY flows are more distinctly different downstream of the piston (left chamber).

In this downstream region, Fig. 7d, which corresponds to the highest Wi tested, shows the development of vortices which are of elastic origin since inertia is very low. Elasticity in fluids is known to induce flow instabilities, see e.g. [68–72]. Although due to the transiency of the problem, with the piston velocity not being constant, it is difficult to precisely describe the vortex shedding dynamics, Fig. 9b shows clear evidence of this process in the $f = 32$ Hz simulation for the IPTT-100 fluid. That figure monitors the radial velocity component at a specific location in the left chamber of the damper and shows that it changes sign multiple times during a damper oscillation period; the frequency of the vortex shedding does not seem to

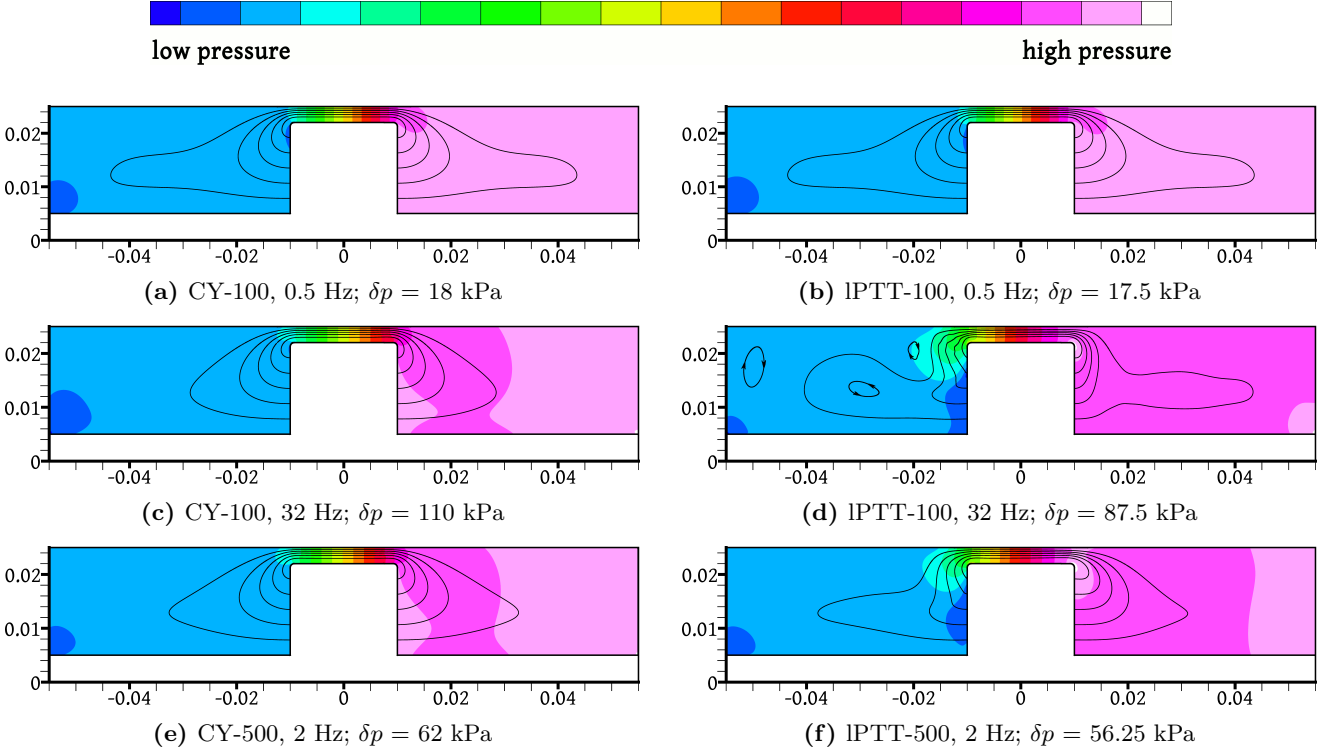


Figure 7: Pressure contours (colour) and instantaneous streamlines (black lines) of the flow inside the damper, for different fluids and frequencies. The piston is moving towards the right with maximum velocity (the snapshots are taken at time $t = 5T + 3T/4$). The step of the pressure contours, δp , is indicated in each case.

be directly related to the damper oscillation frequency. On the contrary, at the lower frequency of $f = 8$ Hz Fig. 9a shows that the fluid velocity at the same location is completely harmonised with the piston motion (compare with the cosine wave drawn in dashed line): the velocity is small when the piston is displaced towards the right, away from the given point ($t \in [(k - 0.25)T, (k + 0.25)T]$ approximately, where k is an integer), becomes large and positive when the piston is displaced towards the left and is approaching the given point and is pushing the fluid of the left compartment towards the gap ($t \in [(k + 0.25)T, (k + 0.5)T]$), and becomes negative when the piston is retracting from its extreme left position and forcing the fluid of the right compartment to flow into the left compartment ($t \in [(k + 0.5)T, (k + 0.75)T]$). In the $f = 32$ Hz case (Fig. 9b) the kinematics of the vortex shedding are superimposed on this mean fluid motion. The $f = 32$ Hz IPTT-100 case was the only one among the cases studied where instabilities were observed. A thorough examination of this phenomenon is beyond the scope of the present paper.

Figures 10 and 11 show snapshots of the distribution of the stress component τ_{rx} for frequencies $f = 0.5$ Hz and $f = 32$ Hz, respectively, for the CY-100 and IPTT-100 fluids. The geometry of the present problem is such that τ_{rx} is by far the most crucial stress component for producing F_{fl} . Figure 10a shows that at low frequencies the IPTT-100 and CY-100 models predict very similar stress distributions when the piston is moving fast. However, when the piston is coming to a halt (Fig. 10b) the CY-100 stresses go to zero because the fluid velocity, and therefore also its gradient, vanish since the inertia of the fluid is very low. For generalised Newtonian fluids such as the CY-100 the stress tensor depends only on the instantaneous velocity gradient which is zero in this case. On the contrary, the PTT stresses depend also on the deformation history and at the time instance shown in Fig. 10b they have not had enough time to relax; they are non-zero and continue to push the piston towards the left (towards the $x = 0$ position), despite the near-zero velocity gradient.

These phenomena are much more pronounced at the $f = 32$ Hz frequency (Fig. 11). Now, when the piston is stopped (Fig. 11b) the PTT stresses are quite high, comparable to those when the piston is moving fast (Fig. 11a). This is because the Deborah number is high (Table 3), i.e. the time scale of the oscillatory piston motion is comparable to the relaxation time of the fluid and the stresses do not have enough time to relax within an oscillation period. On the other hand, the CY stresses again go to zero when the piston stops, a sign that fluid inertia is still quite small even at this high frequency. Concerning the stress distributions

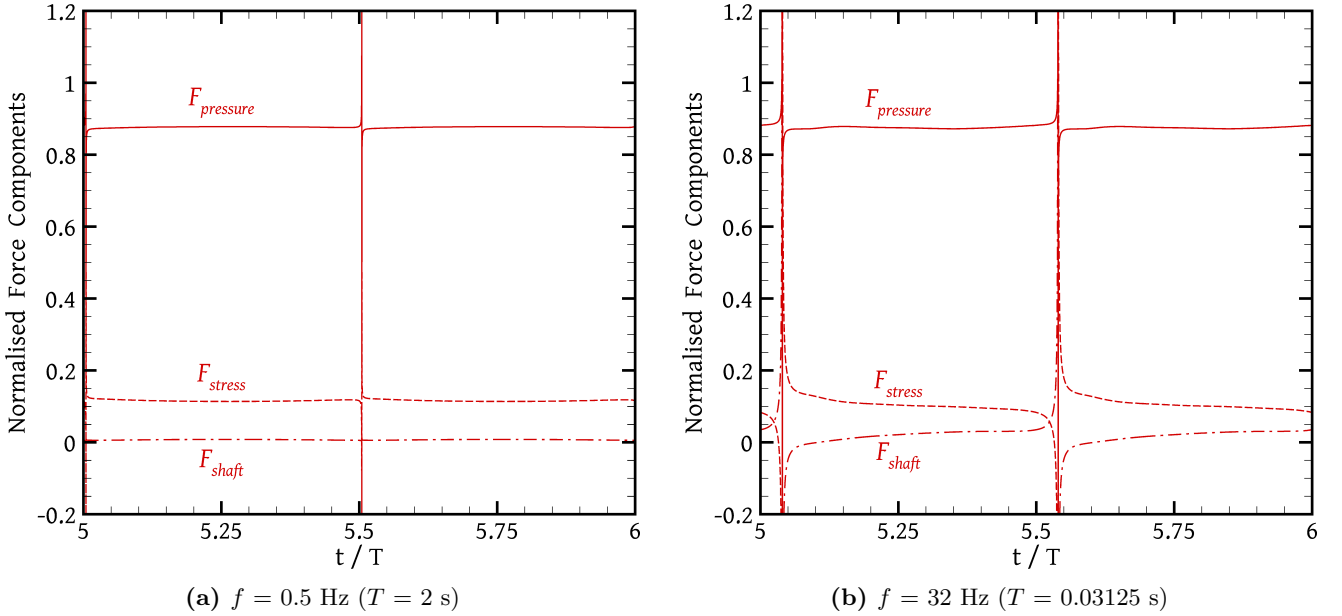


Figure 8: Components of the force F_{fl} , Eq. (17), normalised by $F_{fl}(t)$ itself, for the IPTT-100 fluid, as a function of time normalised by the oscillation period, over the last (6th) period. Continuous line: pressure force on the piston, $\iint_{\text{piston}} -p \underline{n} \cdot \underline{e}_x ds$. Dashed line: force due to viscoelastic stresses on the piston, $\iint_{\text{piston}} \underline{n} \cdot \underline{\underline{\tau}} \cdot \underline{e}_x ds$. Dash-dot line: force due to viscoelastic stresses on the shaft, $\iint_{\text{shaft}} \underline{n} \cdot \underline{\underline{\tau}} \cdot \underline{e}_x ds$. See the description of Eq. (17) for notation. The pressure force on the shaft acts only in the r direction, so it does not contribute to F_{fl} .

at high piston velocities (Fig. 11a), contrary to the $f = 0.5 \text{ Hz}$ case now they are quite different between the IPTT-100 and CY-100 fluids, with the former exhibiting complex patterns.

4.2. Effects of shear-thinning

Shear-thinning plays the most important role in determining the overall force levels. As mentioned, for this flow the most important stress component is τ_{rx} , and consequently the most important type of fluid deformation is shear. Therefore, steady shear diagrams such as that of Fig. 2 can convey a lot of useful information about this flow. This is why the Carreau-Yasuda model is relatively successful in its predictions, especially at low frequencies: in the concept of a generalised Newtonian fluid it is inherently assumed that a steady shear diagram such as Fig. 2 conveys all the information about the fluid rheology.

The importance of shear-thinning is demonstrated in Fig. 12a: even at the low frequency of $f = 0.5 \text{ Hz}$ the force produced by the CY-100 and IPTT-100 fluids when the piston is at $x = 0$ is only 64% and 62%, respectively, of that produced by a Newtonian fluid of 100 Pa s viscosity (N-100). The force reduction due to shear-thinning increases overwhelmingly with increasing frequency; at $f = 32 \text{ Hz}$ these ratios of CY-100 and IPTT-100 forces to N-100 force become 6% and 4.6%, respectively. The force difference between the CY and IPTT fluids will be discussed in Section 4.4.

Figure 12 also shows that while the Newtonian force – displacement loops are elliptical in shape, those of both the PTT and CY models are more “rectangular”, i.e. the force rises sharply as the piston moves away from an extreme position, and remains relatively constant along most of the piston stroke. This is a result of the shear-thinning property of the PTT and CY models: as the piston accelerates, the shear rate $\dot{\gamma}$ increases, but the viscosity η decreases, albeit at a lower pace, (Fig. 2), resulting in a small overall rise of the stress $\tau = \eta \dot{\gamma}$. The exact opposite happens during deceleration of the piston. Therefore, the variation of the force is mild along most of the piston stroke. This is usually a desirable property, as it maximises the absorbed energy for a given force capacity. In this respect shear-thinning fluids such as the CY and PTT behave similarly to viscoplastic fluids [22].

In terms of the force-velocity diagrams (Figs. 6, 13), shear thinning has the effect of reducing the slope of the curves as the velocity increases. On the contrary, for the N-100 fluid the slope of the force curve remains constant at all piston velocities (Fig. 6). Thus, if one wishes to fit the power law (1) to these force-velocity relationships then the exponent n would be $n = 1$ for the Newtonian fluid and $n < 1$ for the CY and PTT fluids.

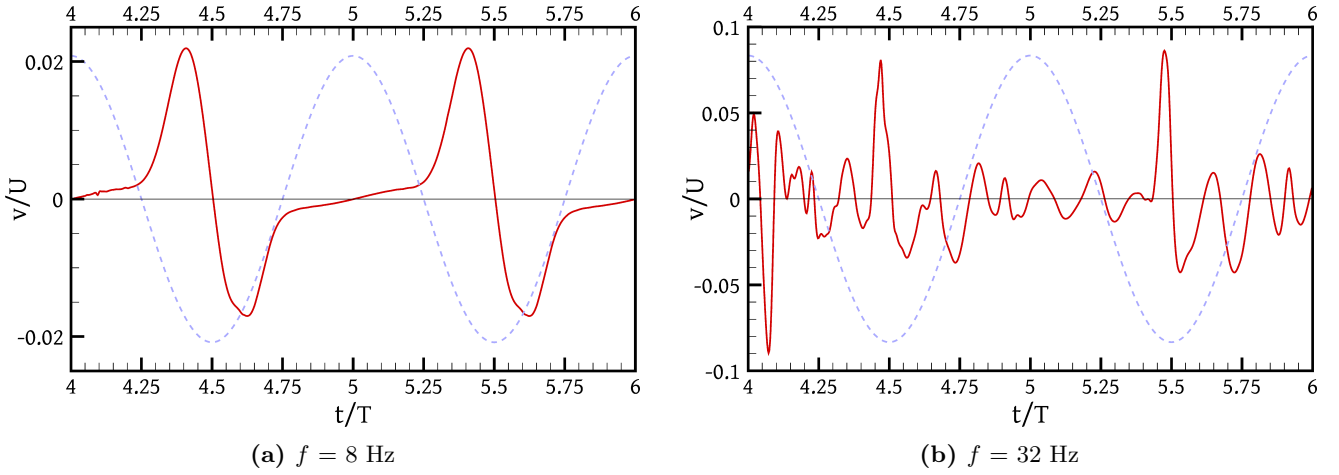


Figure 9: History of the radial (r -) velocity component v of the IPTT-100 fluid at location $x = -35$ mm, $r = 15$ mm, for the $f = 8$ Hz (a) and the $f = 32$ Hz (b) simulations (drawn in continuous line). The velocity v (ordinate) is normalised against the velocity scale U (Table 3), while time (abscissa) is normalised by the oscillation period $T = 1/f$. Also drawn, in dashed line, is a cosine wave, which is in phase with the piston displacement.

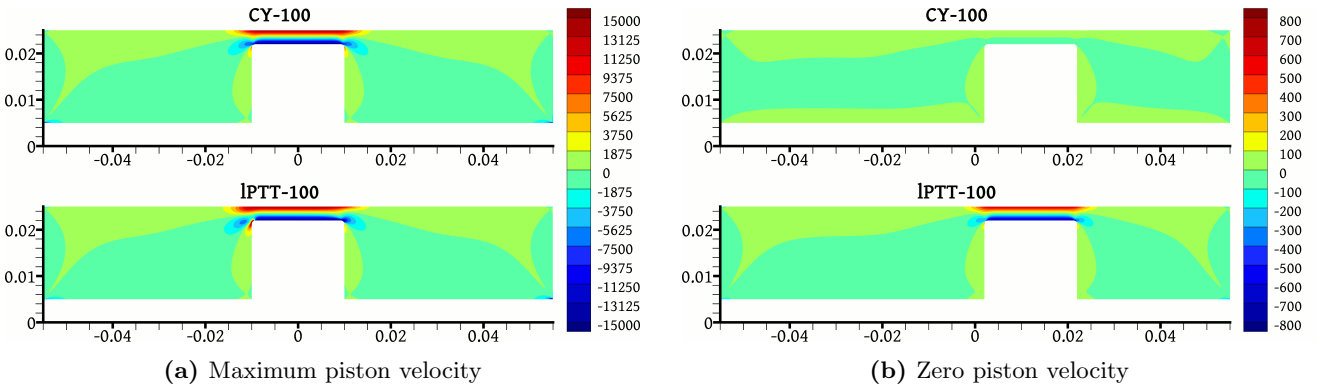


Figure 10: Contours of the $\tau_{r,x}$ stress component, in Pa, for the fluids indicated, at a frequency of $f = 0.5$ Hz. The figures on the left correspond to time $t = 5T + 3T/4$, when the piston moves with maximum velocity towards the right; those on the right correspond to time $t = 6T$, when the piston momentarily stops moving.

Another effect of shear-thinning is that it strengthens the role of inertia by weakening the viscous / viscoelastic stresses. This will be discussed in Sec. 4.3.

4.3. Effects of inertia

As indicated by the Reynolds numbers listed in Table 3, fluid inertia plays only a minor role in this flow. When the fluid is Newtonian, inertia is not at all noticeable due to the high viscosity: force-displacement diagrams are perfectly elliptical (Figs. 4a, 12a) and force-velocity diagrams are lines rather than loops (Figs. 6a, 6b); no hysteresis is observed. On the other hand, some hysteresis, although mild, is evident in the corresponding plots of the CY fluids at $f = 32$ Hz, and inertia is the only mechanism that can be responsible for this. The difference between the Newtonian and CY fluids is that the latter exhibit shear-thinning, which means that at high velocities the viscous forces acting on CY fluid particles are significantly smaller than those acting on the Newtonian fluid particles. Since the force balance is between viscosity, pressure, and inertia, smaller viscous forces implies a more significant role for inertia.

How inertia influences the flow can be observed in the force-displacement and force-velocity diagrams for the CY-100 fluid at $f = 32$ Hz. In Fig. 4c, and in Fig. 6b on the CY-100 curve, one observes that $|F_{fl}(a)| = |F_{fl}(c)| < |F_{fl}(b)|$. In other words, for the same piston displacement and velocity magnitude, the force is greater when the piston is accelerating than when it is decelerating. This is because during acceleration the piston has to accelerate also the surrounding fluid (added mass effect), and fluid inertia makes this harder; during deceleration, on the other hand, the piston also has to decelerate the surrounding fluid which pushes the piston forward due to its inertia, thus aiding to overcome the viscous fluid resistance

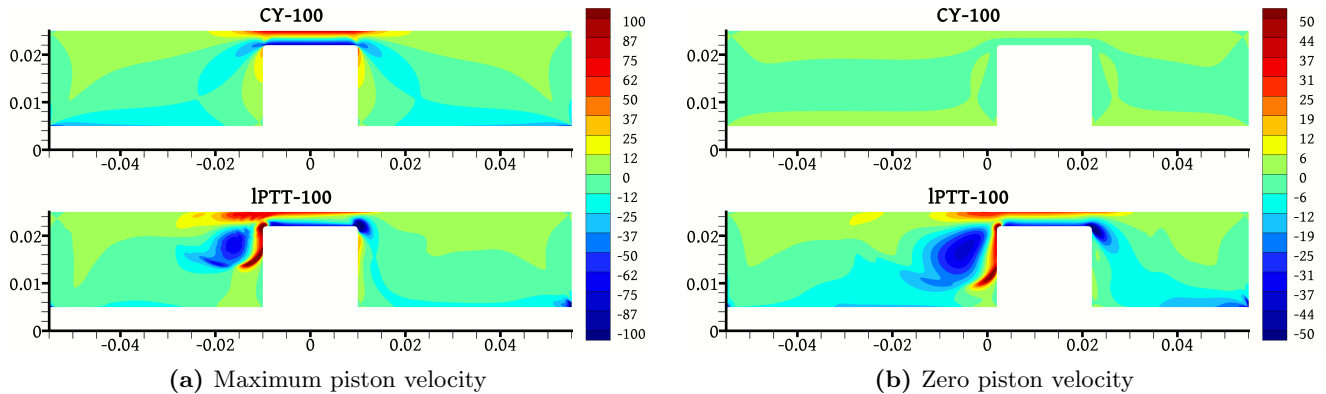


Figure 11: As per Fig. 10, but for a frequency of $f = 32$ Hz. Also, the τ_{rx} contours are in kPa rather than Pa.

and resulting in a smaller overall backwards force. The component of F_{fl} that is related to the fluid inertia is depicted schematically in Fig. 5. Inertia effects are only noticeable at the highest frequency considered: in Fig. 14a one can observe that it is only at $f = 32$ Hz that the loop is stretched more in the +45 degree direction than in the -45 degree direction, and in Fig. 13a it is only at $f = 32$ Hz that the force is plotted as a loop rather than a single line. The highly viscous nature of the fluids does not allow significant inertial effects in this particular application. More pronounced inertial effects were studied in [22].

Inertia effects are not particular to the CY fluid, but concern the PTT fluid as well; however, for the latter things are complicated by the superposition of elasticity effects which in many respects act in an opposite manner to inertia. The discussion is deferred to Sec. 4.4.

4.4. Effects of elasticity

Viscoelasticity is responsible for the “stiffness” aspect of the damper’s behaviour that was described in Sec. 1. In particular, one can notice in Fig. 4i that $|F_{fl}(a)| = |F_{fl}(c)| > |F_{fl}(b)|$, i.e. the fluid reaction force is larger when the piston approaches the extreme positions and smaller when it is moving away from them. This can be attributed to fluid elasticity: the piston motion deforms the fluid, and the latter, being elastic, tends to recover its original shape pushing the piston backwards. In fig. 5b although the piston has reversed its direction of motion compared to Fig. 5a, there was not enough time to completely undo the fluid deformation caused by the preceding rightward piston motion and the elastic component of F_{fl} continues to push the piston towards the left. Thus, when the piston is close to the extremities the elastic component of F_{fl} acts in a spring-like manner, pushing the piston towards the centre of the damper. This is completely at odds with the effect of inertia (Fig. 5). In force-displacement and force-velocity diagrams elastic effects are manifest in the form of a hysteresis that has the exact opposite sense than that of inertia: the force-displacement loops are stretched in the -45 degree direction (Fig. 14b) rather than in the +45 degree direction (Fig. 14a) and the force-velocity loops have a clockwise sense (Fig. 13b) rather than a counterclockwise one (Fig. 13a). This opposite manifestation of inertial effects compared to elastic effects has been observed also in LAOS experiments [73]. Of course, at $f = 32$ Hz inertia effects are also expected to play a role for the IPTT-100 fluid, similarly to the CY-100 case, but for this particular flow they are somewhat masked by the elastic effects which are dominant. Nevertheless, it will be shown below that the weakening of the elastic hysteresis observed at normalised velocity magnitudes greater than 0.5 for $f = 32$ Hz in Fig. 13b compared to $f = 8$ Hz is due to a superposition of an opposed inertial hysteresis.

It would be nice if the observable effect of elasticity could somehow be quantified instead of relying only on qualitative observations. A simple way to do this arises from a decomposition of the fluid force F_{fl} into “viscous” and “elastic” components, which is inspired by an analogous procedure applied in LAOS experiments [74]. For a purely elastic medium, one would expect the force to be a function of only the piston displacement, $F_{fl}(x_p)$, while for a purely viscous medium one would expect it to be a function of only the piston velocity, $F_{fl}(u_p)$. In practice, due to the mixed character of silicone oil, the force-displacement and force-velocity diagrams are hysteretic, meaning that for each piston displacement the force has two distinct values, depending on the piston velocity, and similarly for each piston velocity the force has two distinct values, depending on the piston displacement. The force therefore depends on both the piston displacement

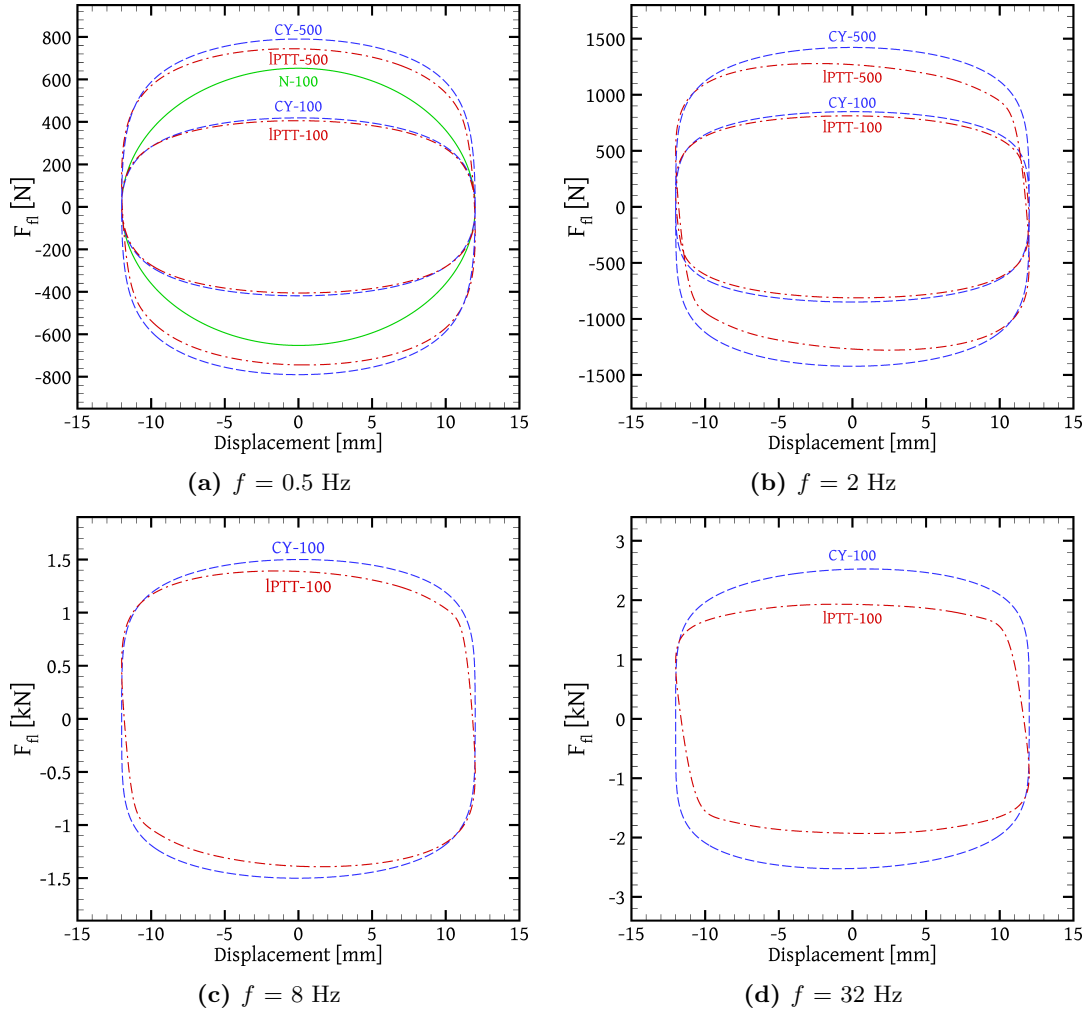


Figure 12: Force F_{fl} (Eq. (17)) versus piston displacement plots, for each of the oscillation frequencies selected for the simulations. Each plot contains the results of all fluids tested at that particular frequency, except for the N-100 fluid which is only plotted in (a) for clarity.

and velocity, $F_{fl}(x_p, u_p)$. A simple way to split this force is the following:

$$F_{fl}(x_p, u_p) = \frac{F_{fl}(x_p, u_p) + F_{fl}(x_p, -u_p)}{2} + \frac{F_{fl}(x_p, u_p) - F_{fl}(x_p, -u_p)}{2} \quad (19)$$

If the periodic state has been reached, then from symmetry considerations it follows that $F_{fl}(-x_p, -u_p) = -F_{fl}(x_p, u_p)$ (the forces at instances (a) and (c) of Fig. 5 are of equal magnitude but opposite sense), which also means that $F_{fl}(x_p, -u_p) = -F_{fl}(-x_p, u_p)$. Substituting this last equation in Eq. (19) we obtain

$$F_{fl}(x_p, u_p) = F_{fl}^e(x_p) + F_{fl}^v(u_p) \quad (20)$$

where

$$F_{fl}^e(x_p) \equiv \frac{F_{fl}(x_p, u_p) + F_{fl}(x_p, -u_p)}{2} \quad (21)$$

$$F_{fl}^v(u_p) \equiv \frac{F_{fl}(x_p, u_p) - F_{fl}(-x_p, u_p)}{2} \quad (22)$$

The reason why the component F_{fl}^e can be considered to be a function of only x_p (for the given operating conditions) is that expression (21) is an even function of u_p , i.e. it has the same value at point (x_p, u_p) as it has at the point $(x_p, -u_p)$. Thus, whereas in a plot of F_{fl} versus x_p , for each piston displacement x_p there are two distinct F_{fl} values, one corresponding to the piston moving towards the right with velocity u_p and one corresponding to it moving towards the left with velocity $-u_p$, in a plot of F_{fl}^e versus x_p these two values coincide, and the plot is a single line rather than a loop (no hysteresis). Thus F_{fl}^e is completely determined

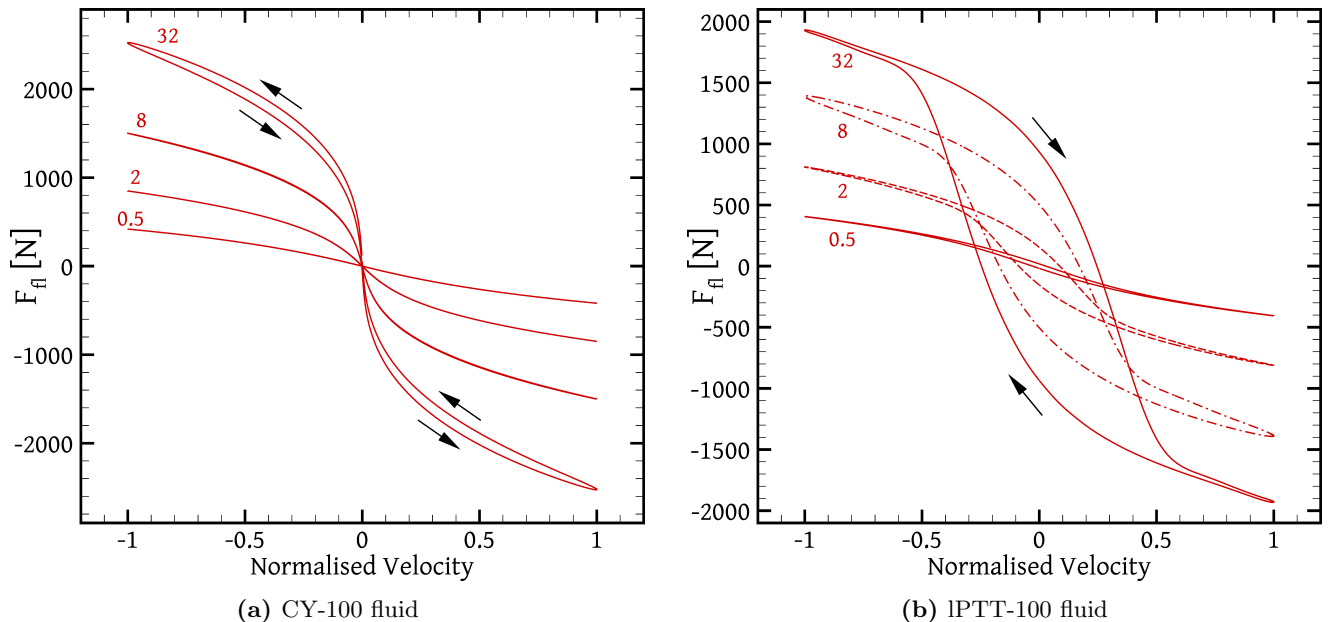


Figure 13: Diagrams of force F_{fl} (Eq. (17)) versus piston velocity, the latter divided by its maximum value U_p (Eq. (5), listed in Table 3 for each frequency) for all the tested frequencies $f = 0.5, 2, 8$ and 32 Hz; the left diagram (a) is for the CY-100 fluid, and the right diagram (b) is for the IPTT-100 fluid.

by the piston displacement x_p , as for a force of purely elastic origin. The averaging of $F_{fl}(x_p, u_p)$ and $F_{fl}(x_p, -u_p)$ in expression (21) can be assumed to cause a cancellation of the viscous effects of the opposite velocities u_p and $-u_p$, leaving only the elastic effect of the displacement x_p on the force F_{fl} . Hence F_{fl}^e will be termed the “elastic” component of F_{fl} .

In exactly the same way, the “viscous” component F_{fl}^v , eq. (22), of F_{fl} , comes from averaging the values $F_{fl}(x_p, u_p)$ and $F_{fl}(-x_p, u_p)$ to eliminate the opposite elastic effects of the displacements x_p and $-x_p$, leaving only the viscous effect of the piston velocity u_p . The expression (22) is an even function of x_p and thus the plot of F_{fl}^v versus u_p is a single line, not a loop, as for a force of purely viscous origin.

Putting these ideas to practice, normalised diagrams of F_{fl}^e versus displacement and of F_{fl}^v versus velocity are plotted in Figs. 15a and 15b, respectively, for all cases. The diagrams are plotted only for positive displacement and velocity, due to symmetry ($F_{fl}^e(-x_p) = -F_{fl}^e(x_p)$ and $F_{fl}^v(-u_p) = -F_{fl}^v(u_p)$). It is noted that, from Eq. (21), the curve of F_{fl}^e versus displacement is just the average between the upper and lower branches of the F_{fl} vs. displacement loop, and similarly, from Eq. (22), the curve of F_{fl}^v vs. velocity is just the average between the upper and lower branches of the F_{fl} vs. velocity loop. Figure 15a shows that the elastic component F_{fl}^e is quite small over most of the piston stroke but increases sharply as the piston approaches an extreme position. Concerning the viscous component, Fig. 15b shows that as the velocity u_p increases the magnitude of the derivative dF_{fl}^v/du_p decreases, which is directly related to the shear-thinning property of the fluid. In general, this manifestation of shear-thinning becomes more pronounced as either the oscillation frequency or the fluid relaxation time increases.

One possible measure of the elastic character of the fluid force F_{fl} is the ratio of the maximum absolute value of F_{fl}^e to the maximum absolute value of F_{fl} . The value of this ratio is given in Table 6 for all cases. It can reach quite high values – nearly 0.5 for the IPTT-100, $f = 32$ Hz case. From Fig. 15a, the maximum absolute value of F_{fl}^e occurs at the extreme displacements $x_p = \pm\alpha$, where in fact $F_{fl}^e = F_{fl}$ because $F_{fl}^v = 0$ (this follows from the definition (22) combined with the fact that $u_p = 0$ at $x_p = \pm\alpha$ and the aforementioned symmetry condition $F_{fl}(x_p, -u_p) = -F_{fl}(-x_p, u_p)$). If the simulation cases are sorted according to the values of this ratio then the order is roughly the same as that which results from sorting according to the Wi or De numbers (Table 3).

The large values of the ratio $\max(F_{fl}^e)/\max(F_{fl})$ may give an exaggerated picture about the overall effect of elasticity, since F_{fl}^e has very small values over most of the piston stroke and only increases close to

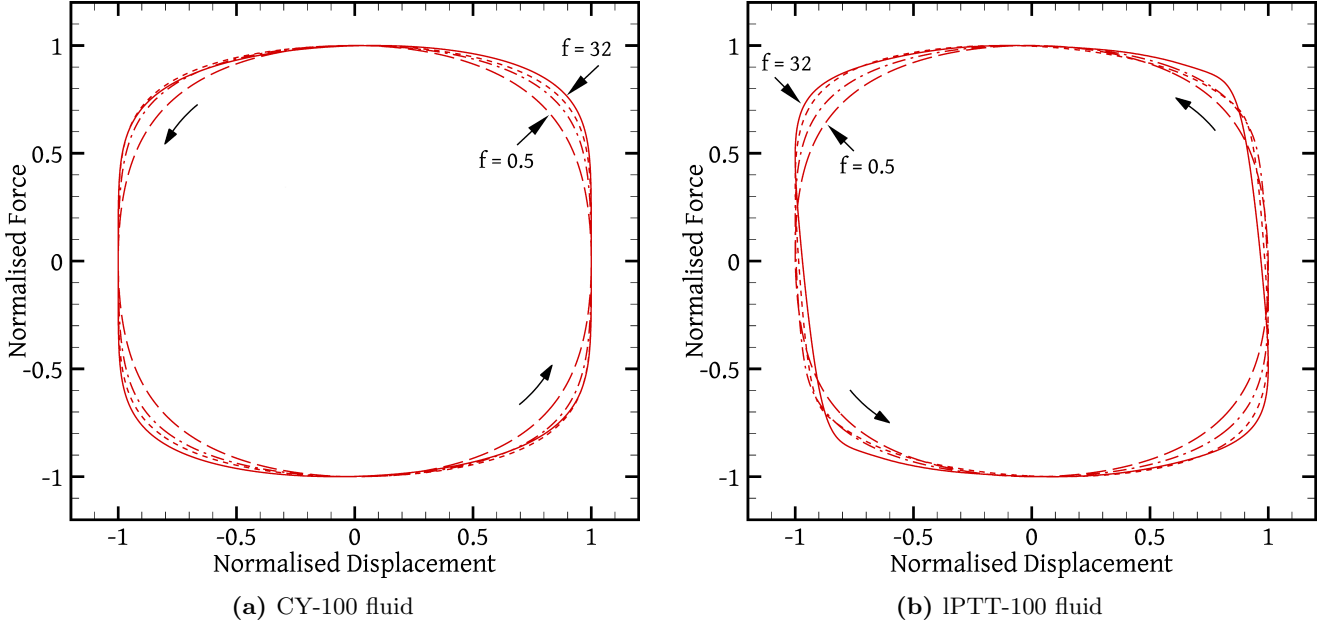


Figure 14: Diagrams of force F_{fl} (Eq. (17)) versus displacement during the last (sixth) period simulated, normalised by their maximum values in each case, for all the tested frequencies $f = 0.5$ (long dashes), 2 (dash-dot), 8 (short dashes) and 32 (solid) Hz; the left diagram (a) is for the CY-100 fluid, and the right diagram (b) is for the IPTT-100 fluid.

Table 6: Ratios of maximum magnitude of F_{fl}^e (Eq. (21)) over maximum magnitude of F_{fl} and of W_{fl}^e over W_{fl} (Eqs. (24) and (23)), expressed as percentages, for various cases. The numbers in parentheses correspond to the line printed with long dashes in Fig. 16.

Fluid	f [Hz]	$\frac{\max(F_{fl}^e)}{\max(F_{fl})}$ [%]	W_{fl}^e/W_{fl} [%]
IPTT-100	0.5	4.5	0.33
	2	19.0	0.67
	8	36.3	2.12
	32	48.4 (52.2)	2.08 (3.18)
IPTT-500	0.5	17.0	0.91
	2	38.1	2.76

$x = \pm\alpha$ (Fig. 15a). A better picture can be obtained by comparing the integrals

$$W_{fl} \equiv \oint F_{fl} dx_p \quad (23)$$

and

$$W_{fl}^e \equiv 2 \int_{x_p=0}^{x_p=\alpha} F_{fl}^e dx_p \quad (24)$$

The integral W_{fl} (23) is the work done by the fluid force F_{fl} during an oscillation cycle, which is the energy dissipated into heat. Since the elastic component F_{fl}^e exhibits no hysteresis when plotted against x_p (its plots in Fig. 15a are single lines and not loops), its net work during a full oscillation is zero, $\oint F_{fl}^e dx_p = 0$. Hence, all of the energy dissipation occurs through the viscous component F_{fl}^v :

$$\oint F_{fl} dx_p = \oint (F_{fl}^v + F_{fl}^e) dx_p = \oint F_{fl}^v dx_p + \oint F_{fl}^e dx_p = \oint F_{fl}^v dx_p + 0$$

However, F_{fl}^e causes storage and release of energy within an oscillation cycle. As the piston approaches an extreme position, F_{fl}^e opposes this motion and converts some of the supplied energy into potential energy in

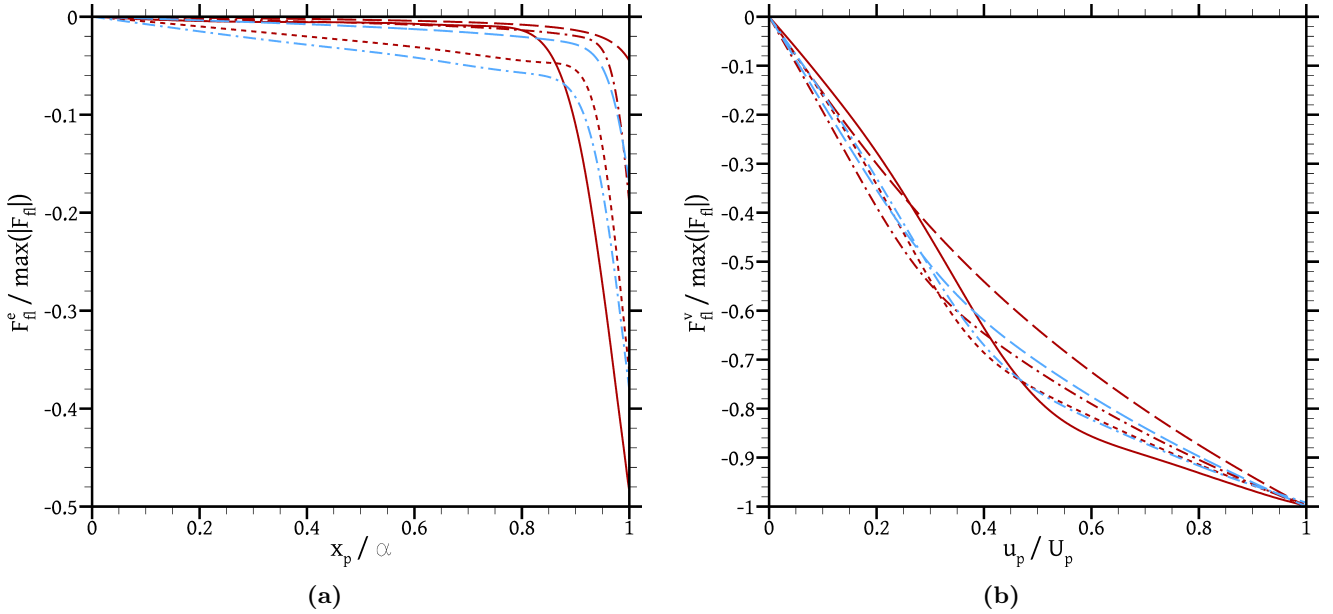


Figure 15: (a) Elastic force component F_{fl}^e (Eq. (21)), normalised by the maximum magnitude of F_{fl} , against piston displacement normalised by the oscillation amplitude α . (b) Viscous force component F_{fl}^v (Eq. (22)), normalised by the maximum magnitude of F_{fl} , against normalised piston velocity (u_p/U_p , Eq. (5)). The dark red lines correspond to the IPTT-100 fluid, and the light blue lines to the IPTT-500 fluid. Line style denotes the oscillation frequency: $f = 0.5$ (long dashes), 2 (dash-dot), 8 (short dashes), and 32 Hz (continuous).

the form of elastic energy of the fluid. This energy is then released as the piston retracts from the extreme position, when F_{fl}^e is pushing it along. The energy storage during an oscillation cycle, omitting the equal energy release, is given by the integral W_{fl}^e , Eq. (24). Thus the ratio W_{fl}^e/W_{fl} , given in Table 6 for the various cases, is an indicator of the importance of elastic effects. It can be seen from the low values of this ratio in Table 6 that the action of the damper is mostly dissipative, with the largest energy storage recorded at about 3%.

Interestingly, the ratio W_{fl}^e/W_{fl} for the IPTT-500, $f = 2$ Hz case is significantly larger than for the IPTT-100, $f = 32$ Hz case for which the Wi and De numbers are highest. This is connected to the fact that F_{fl}^e for the latter case is very small up to $x_p \approx 0.8\alpha$ (Fig. 15a), and one cannot help but wonder whether this is due to inertia effects masking the elastic effects. This can be checked by plotting F_{fl}^e for the corresponding CY-100, $f = 32$ Hz case for which there is no elasticity. This plot, in Fig. 16, shows that the “elastic” component F_{fl}^e is in fact non-zero, and that its direction (the sign of F_{fl}^e in Fig. 16) is exactly the opposite of what would be expected of an elastic force: as the piston moves towards $x_p = \alpha$, F_{fl}^e keeps pushing it forward instead of opposing the motion. Obviously, F_{fl}^e is in this case the inertial component of the total force F_{fl} (Fig. 5). One notices also in Fig. 16 that in the CY-100 case F_{fl}^e increases linearly with the piston displacement x_p . This is not surprising, and shows that the inertial component of the force is proportional to the piston acceleration (which is in phase with the displacement, comparing Eqs. (4) and (16)); the fluid acceleration, and hence the required force, follows that of the piston. In the IPTT-100 case (for $f = 32$ Hz, which is the only case when inertia is noticeable) F_{fl}^e is the net sum of the elastic and inertial components, which oppose each other. Both components store energy to release it later (elastic potential energy in the case of the elastic component and fluid kinetic energy in the case of the inertial component) each with a net work of zero during a full oscillation, but as one is storing the other is releasing and vice versa. If we want to isolate only the elastic part of the force, we can assume that the inertial part is the same as for the CY-100 fluid at the same frequency (which has no elastic part) and subtract it from the whole, i.e. the purely elastic component of F_{fl}^e for a IPTT fluid can be approximated as $F_{fl}^e(\text{IPTT}) - F_{fl}^e(\text{CY})$. This is plotted in Fig. 16 (line with long dashes) and it may be seen to no longer be negligible for displacements $x_p/\alpha < 0.8$ compared, for example, to the IPTT-100, $f = 8$ Hz case. Also, in Table 6 the corresponding metrics are printed in parentheses, and the W_{fl}^e/W_{fl} ratio can be seen to now be the highest among all cases, in correspondence with that case’s Wi and De numbers’ ranking.

Another phenomenon that must be attributed to the elasticity of the fluid is the systematically lower F_{fl}

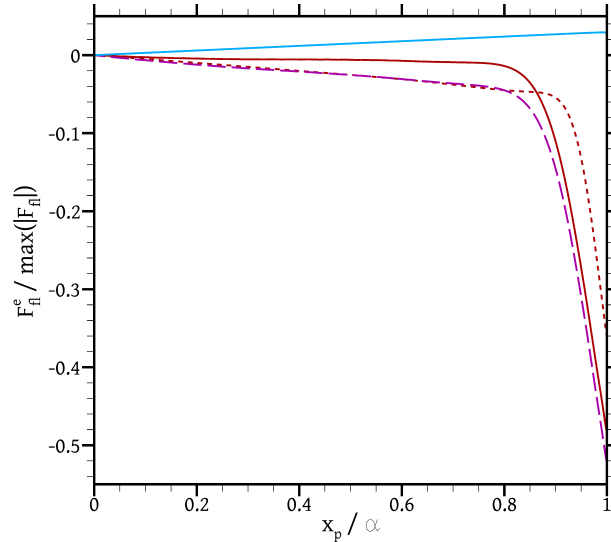


Figure 16: The force component F_{fl}^e , Eq. (21), normalised by the maximum value of F_{fl} , against normalised piston displacement x_p/α , for the following cases: IPTT-100 at $f = 32$ Hz (continuous dark red line), IPTT-100 at $f = 8$ Hz (short dashes, dark red), and CY-100 at $f = 32$ Hz (continuous light blue line). The purple line of long dashes corresponds again to the IPTT-100, $f = 32$ Hz case where, however, from its F_{fl}^e force the corresponding component F_{fl}^e of the CY-100, $f = 32$ Hz case has been subtracted (normalisation is again by the maximum F_{fl} value of the IPTT-100, $f = 32$ Hz case).

values observed for the PTT fluids compared to the corresponding CY fluids, at the same frequencies. Figure 12 and Table 3 show that the higher the Deborah number is, the lower F_{fl} is for a PTT fluid compared to the CY fluid of the same nominal viscosity, at the same frequency. Since the CY parameters have been fitted so that the CY fluids' behaviour exactly matches that of the corresponding PTT fluids in steady shear (Fig. 2), this observation indicates that for the PTT fluids shear-thinning is not the only factor that causes a force reduction compared to Newtonian fluids, but there is an additional factor that cannot be any other than elasticity. To investigate this, in Fig. 17 we plot the distribution of τ_{rx} on the horizontal surface of the piston, i.e. along its length excluding the rounded corners, at maximum piston velocity towards the right, for both the CY-100 and IPTT-100 fluids at the $f = 32$ Hz frequency for which the force difference between the two fluids is the largest. The stresses are negative, pushing the piston towards the left. As mentioned, this τ_{rx} distribution is mostly the cause of F_{fl} both directly and indirectly through the pressure difference that it generates across the piston. Figure 17 shows that whereas for the CY fluid τ_{rx} is constant over most of the piston length, for the PTT fluid this stress component increases in magnitude as one moves downstream (i.e. towards the left). At the left end of the piston the PTT stress magnitude has not yet caught up with the CY stress levels; overall, τ_{rx} has larger magnitude for the CY fluid, resulting in a larger force F_{fl} .

These observations concerning τ_{rx} can be explained by looking at velocity profiles across the gap, from the piston surface to the outer casing, such as those drawn in Fig. 18. Figure 18a shows that once the CY fluid enters the gap it very quickly acquires its fully developed velocity profile, a profile which is typical of a shear-thinning generalized Newtonian fluid, exhibiting flatness away from the walls and a steep gradient close to the walls. In contrast, Fig. 18b shows that the flow of the PTT fluid that enters the gap evolves much more slowly and does not reach a fully developed profile before the fluid exits at the other side of the gap. The PTT profile is initially more “pointed”, near the gap entrance, and evolves towards a flatter profile, more reminiscent of the CY profile, as the fluid moves downstream. A more pointed profile entails a less steep velocity gradient at the piston wall, hence the lower τ_{rx} magnitudes for the PTT fluid compared to the CY fluid. Similar observations have been reported for contraction flows of viscoelastic fluids (both shear-thinning and non-shear-thinning (Boger) fluids), for which both experimental and numerical studies [75–77, 68–70] have shown that the fluid velocity along the channel centreline is maximum at the contraction entrance and drops towards a limit value as the fluid moves downstream.

This different behaviour between the two fluids reflects the different importance of convective terms in their respective governing equations. For the CY fluid, the convective terms of the momentum equation (12) are not significant due to the low value of Re , and therefore the flow is elliptic in character and adapts

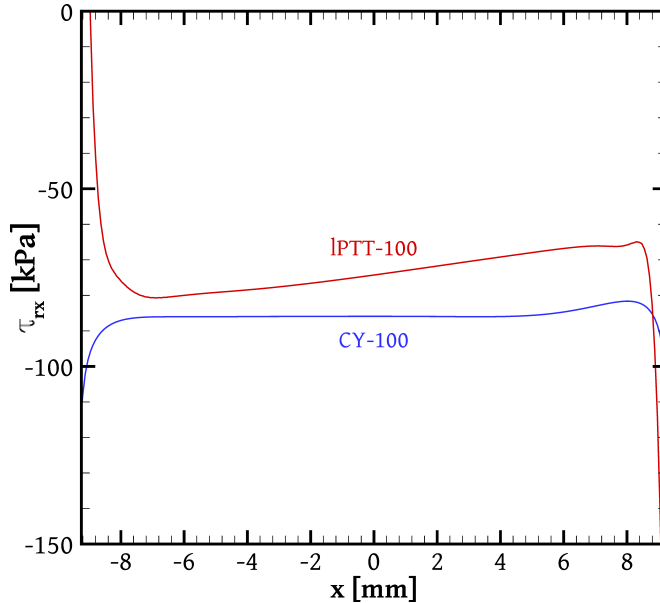


Figure 17: Distributions of the τ_{rx} stress component along the horizontal surface of the piston for the CY-100 (blue) and IPTT-100 (red) fluids, at a time instance when the piston is moving with maximum velocity towards the right; the oscillation frequency is $f = 32$ Hz.

almost instantaneously to its local surroundings, thus resulting in a very short development length in the gap. For the PTT fluid, the convective terms of the momentum equation are insignificant as well, but now the constitutive equation (13) also includes convection terms which are quite important and make a fluid particle’s state heavily dependent on its flow history and not only on its surroundings. This results in a large development length that essentially stretches throughout the gap. To get a better feel of this, one can compare the average time that a fluid particle spends travelling along the gap against the relaxation time of the fluid. At maximum piston velocity, the mean relative velocity between the fluid and the piston is U , listed in Table 3 for the various cases. Dividing the gap length L_p (Table 1) by this velocity gives the average time that it takes for a fluid particle to cross the gap (at maximum piston velocity), $T_p = L_p/U$ say. Dividing this time with the relaxation time of the fluid, we get the following results: for the IPTT-100 fluid, $T_p/\lambda = 12.5$ ($f = 0.5$ Hz), 3.1 ($f = 2$ Hz), 0.8 ($f = 8$ Hz) and 0.2 ($f = 32$ Hz); for the IPTT-500 fluid, $T_p/\lambda = 2.1$ ($f = 0.5$ Hz) and 0.5 ($f = 2$ Hz). Therefore, in the higher De number cases considered, the particle travel time is smaller than the relaxation time of the fluid, and a fluid particle does not have enough time to reach a “steady state” until it reaches the exit of the gap.

The conclusion is then that viscoelastic flow can entail large development lengths in the gap, and simplified one-dimensional analyses such as those mentioned in Sec. 1 may lead to significant underestimation of the force.

4.5. Applied force

Since the damper geometry and kinematics are known, the shaft-piston mass and acceleration in Eq. (15) can be calculated and the equation solved for the applied force F_{ap} . Neglecting the friction force F_{fr} leads to

$$F_{ap} = M_p a_p - F_{fl} \quad (25)$$

The fluid reaction force F_{fl} has been computed and the results were presented in the preceding sections. The mass M_p of the piston-shaft assemblage can be estimated at about 0.3 kg from the geometrical dimensions and assuming a material density of 8000 kg/m³ (steel). From Eq. (16) it is seen that the extra component of F_{ap} required to overcome the inertia of the piston, $M_p a_p$, is in phase with the piston displacement (4). The plot of $M_p a_p$ versus piston displacement is a straight line of slope $-M_p \omega^2$ (Fig. 19a). Since the plot collapses to a single line rather than a loop, the net work of this force component is zero, causing no energy dissipation. By inverting the plots of F_{fl} of Fig. 12 and superimposing the corresponding plots of $M_p a_p$, Fig. 19a, we obtain the plot of F_{ap} , Eq. (25), shown in Fig. 20a.

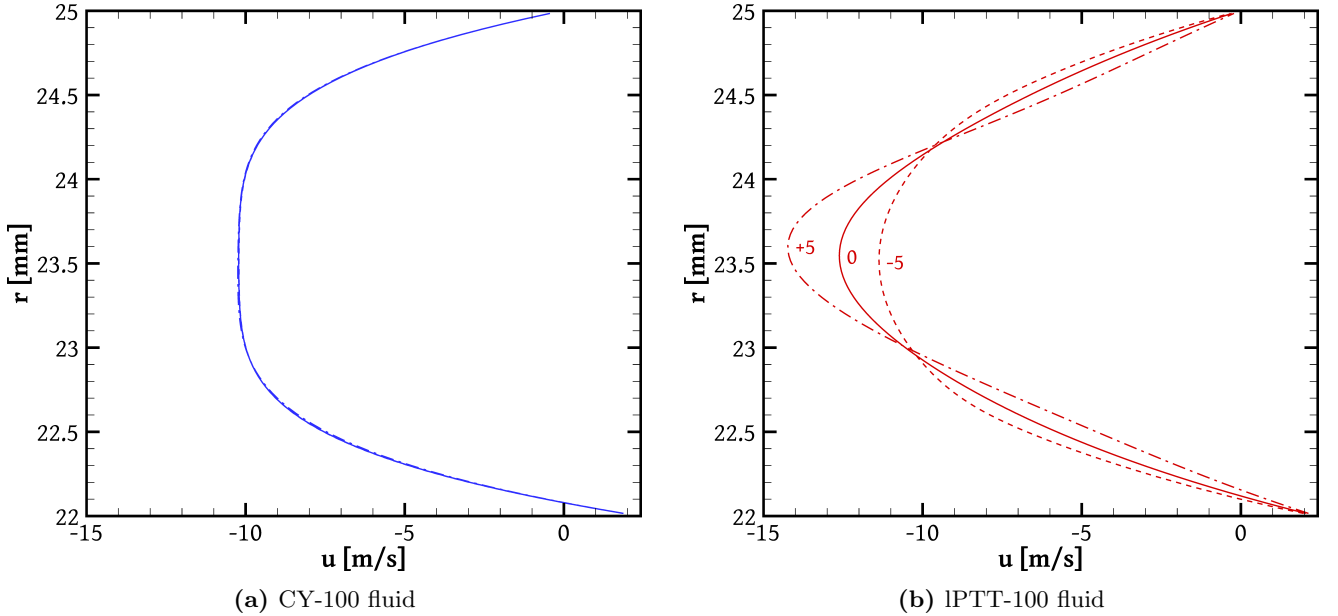


Figure 18: Profiles of the x -component of fluid velocity across the gap, at a time instance when the piston is moving towards the right with maximum velocity, with its midpoint at $x = 0$, for the CY-100 (a) and IPTT-100 (b) fluids. The frequency is $f = 32$ Hz. Three profiles are plotted in each case: at halfway along the piston ($x = 0$, solid line), at 5 mm upstream ($x = +5$ mm, dash-dot line), and at 5 mm downstream ($x = -5$ mm, dashed line). The profiles nearly coincide in the CY-100 case (a).

Similarly, we can draw F_{ap} versus piston velocity in Fig. 20b by inverting the plot of F_{fl} in Fig. 13b (to account for the minus sign in Eq. (25)) and superimposing the plot of $M_p a_p$ shown in Fig. 19b. Evidently, at $f = 32$ Hz the superposition of the inertial component causes a hysteresis inversion, from elastic-type to inertia-type, when the magnitude of the normalised velocity is greater than 0.5 (note that due to the inversion of Fig. 13b the sense of the hysteresis has also been inverted: elastic hysteresis is now counterclockwise and inertial hysteresis is clockwise). At low velocities (when the piston is near the extremities) the hysteresis remains elastic. At lower frequencies the $M_p a_p$ term is much smaller due to the acceleration a_p being proportional to ω^2 (Eq. (16)) and hence to the square of the frequency, and the piston inertia is not felt much.

The plots of F_{ap} shown in Fig. 20 are in qualitative agreement with experimental data for viscous dampers found in the literature [14–16], and even for magnetorheological dampers [24, 3, 20, 8, 25] (these employ elastoviscoplastic fluids, but plasticity has similar effects to shear-thinning as far as the damper force is concerned). In these studies there is a prominent elastic hysteresis at low velocities in force-velocity diagrams, which is not predicted by simulations with the Carreau-Yasuda model. Hence we only plotted F_{ap} as predicted by the PTT model, which accounts for all fluid properties, viscosity, elasticity, and inertia.

4.6. Using a silicone oil of lower viscosity

For completeness, we briefly investigate the consequences of using a silicone oil whose viscosity lies significantly below the high range on which this investigation has focused. Lower viscosity is related to lower relaxation times, and thus one may expect that elastic effects will become negligible. However, these effects do not depend solely on the relaxation time but also on the geometrical / kinematic parameters of the problem, as expressed in the definitions of the Weissenberg and Deborah numbers. In order to achieve a similar response to that of a high-viscosity oil damper from a damper employing an oil of lower viscosity, the gap width of the latter would have to be reduced as otherwise the force would be too weak due to the low viscosity. The reduced gap width will partially counterbalance the reduction in Wi due to the lower relaxation time (De will be unaffected).

To investigate this, we performed a couple of simulations, at $f = 2$ and 32 Hz, respectively, on the intermediate grid 2 (Table 4), using a fluid labelled “IPTT-10” with parameters $\eta_0 = 10$ Pas, $\lambda = 0.7$ ms and $\epsilon = 0.10$. The relaxation time was chosen on the following basis, since detailed characterisations such as those available for the high-viscosity oils were not found: the viscosity $\eta_0 = 10$ Pas is still high enough

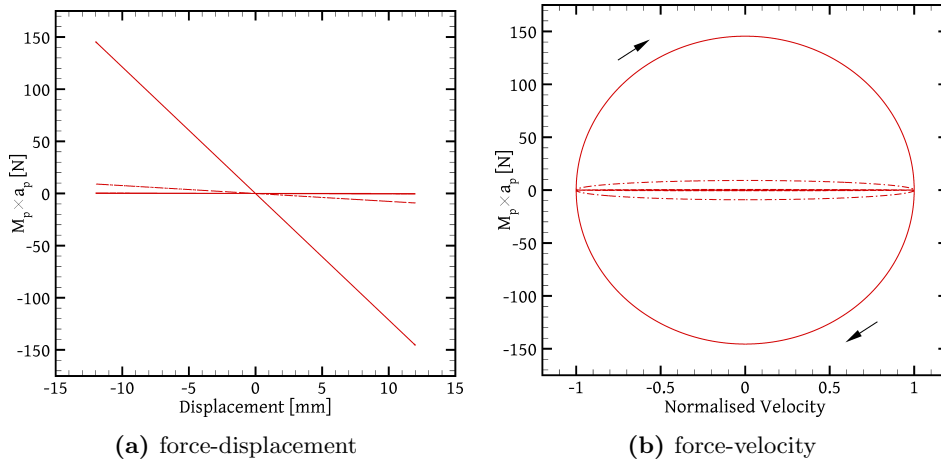


Figure 19: Mass of the shaft-piston assemblage M_p times its acceleration a_p , versus piston displacement (a) or velocity (b) at various oscillation frequencies: $f = 0.5$ Hz (solid line), 2 Hz (dashed line), 8 Hz (dash-dot line) and 32 Hz (solid line, again). At $f = 0.5$ and 2 Hz, $M_p a_p$ is very small and the corresponding lines nearly coincide and are horizontal.

such that the polymer chains are entangled [11] in which case both the reptation time of the polymer chains, which can be used as an approximation to the fluid relaxation time [78], and the zero-shear viscosity are proportional to the molecular weight raised to the power 3.4 [79]. In [11] detailed relaxation spectra are given for three silicone oils of zero-shear viscosities η_0 of 60, 100, and 500 Pas from which Eq. (11) gives average relaxation times λ of 4.2, 10.5 and 40.4 ms, respectively. These values do not deviate substantially from the theoretical proportionality between viscosity and relaxation time, so that it is realistic to select a value of $\lambda = 0.7$ ms for the IPTT-10 fluid by determining the proportionality constant from the closest experimental data pair of $\{\eta_0 = 60 \text{ Pas}, \lambda = 4.2 \text{ ms}\}$. The PTT parameter $\epsilon = 0.10$ was set such that the steady shear viscosity of IPTT-10 compares well against available experimental data (Fig. 21). We note that comparison of the IPTT-10 curve in Fig. 21 against the experimental data shows that for low viscosity silicone oils even the linear PTT model predicts an excessive rate of shear thinning.

To counteract the reduction of viscosity, the gap width was reduced to half (1.5 mm) by enlarging the piston radius to 23.5 mm (the rest of the damper dimensions are unaltered, as in Table 1). This modification was based on the following simple reasoning: given that the radius difference between the piston and the cylinder is small, the cross-sectional area of the gap, A_g say, can be assumed to be proportional to the gap width h . Then, from continuity, the fluid velocity in the gap is inversely proportional to this area and therefore to h . The shear stress τ_{rx} on the piston surface along the gap is then assumed to be proportional to $\eta_0 U / (h/2) \approx \eta_0 U_f / (h/2)$ which is proportional to h^{-2} . Next we consider the force balance on the fluid in the gap, neglecting its inertia: the viscous force, τ_{rx} times the area of the piston and cylinder surrounding the gap, is balanced by the pressure force $\Delta p \times A_g$ where Δp is the pressure difference between the left and right damper compartments. Therefore, Δp is proportional to τ_{rx} / A_g which is proportional to h^{-3} . The pressure component dominates F_{fl} (Fig. 8) and so we also expect $F_{fl} \sim h^{-3}$. Thus by reducing the gap width to half we would expect an 8-fold increase in the force if we used the same fluid, so that using a fluid with 10 times smaller viscosity, such as the IPTT-10 compared to the IPTT-100, we may expect similar levels of force. This analysis depends on several simplifications, one of which is to neglect the effect of shear-thinning. The consequences will be seen below.

The narrowing of the gap and the associated rise of the fluid velocity therein result in large characteristic shear rates $\dot{\gamma}_c$ of 1658 s^{-1} at $f = 2$ Hz and 26532 s^{-1} at 32 Hz. This compensates somewhat for the low value of λ as far as $Wi \equiv \lambda U / H = \lambda \dot{\gamma}_c$ is concerned, resulting in $Wi = 1.16$ and 18.6 for $f = 2$ and 32 Hz, respectively, which is not vastly smaller than the corresponding values for the IPTT-100 fluid. The De number, on the other hand, is quite small: 0.0014 ($f = 2$ Hz) and 0.0224 ($f = 32$ Hz). Concerning shear-thinning, the ratio $\eta(\dot{\gamma}_c) / \eta_0$ is 0.840 ($f = 2$ Hz) and 0.222 ($f = 32$ Hz), significantly larger than the corresponding values for the IPTT-100 fluid. This reflects the fact that shear-thinning is less pronounced and its onset occurs at higher shear rates for lower viscosity silicone oils compared to higher viscosity ones (Figs. 2 and 21). Finally, concerning inertia, we have $Re_c = 0.11$ ($f = 2$ Hz) and 6.71 ($f = 32$ Hz) which is

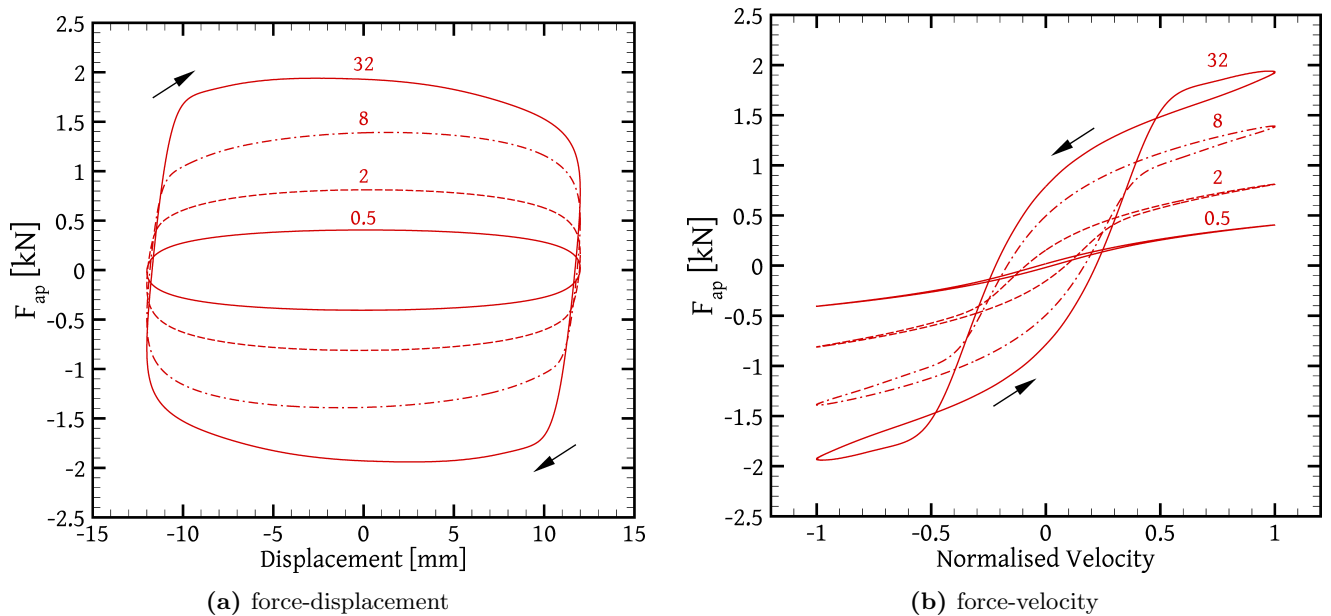


Figure 20: Diagrams of applied force F_{ap} , Eq. (25), versus piston displacement (a) and versus normalised piston velocity (b) for the IPTT-100 fluids, for all the tested frequencies $f = 0.5, 2, 8$ and 32 Hz.

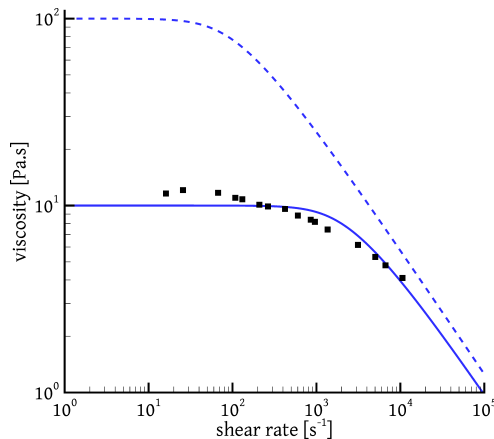


Figure 21: Variation of steady shear viscosity with shear rate for the IPTT-10 (continuous line) and IPTT-100 (dashed line) fluids, along with experimental measurements for a 12.5 Pa.s silicone oil from [10] (■).

significantly larger than for IPTT-100 and thus a more noticeable role is expected of inertia⁵.

Figure 22a shows that at the low frequency of $f = 2$ Hz elastic effects are hardly noticeable⁶; the hysteric loop almost collapses to a single curve. Shear-thinning appears to be weak as well, with the slope of the curve not changing significantly at higher velocities. On the other hand, Fig. 22b shows a clear elastic hysteric loop at low velocities, i.e. when the piston is close to the extremities. At higher velocities the hysteresis changes sense and becomes inertial. As explained in Appendix B, hysteresis reversals can originate also from nonlinearities in the elastic behaviour, but in the present case we believe that they are caused by fluid inertia; Fig. 22c shows that the “elastic” component F_{fl}^e pushes the piston towards the extremities over nearly all of the stroke, and only very close to the extremities does it act in a spring-like manner pushing it away from the extremities. F_{fl}^e varies almost linearly with x_p in the inertial region, as we saw also for the CY-100 fluid in Fig. 16. Also, the relatively high value of $Re_c = 6.71$ suggests that inertial effects should be

⁵Note, however, that the IPTT-10 geometry differs slightly from that of the IPTT-100 and IPTT-500 simulations, and comparing Re_c , De and Wi values between different geometries is not a completely valid way of assessing the relative importance of the effects that these numbers quantify (see our previous publication [22]).

⁶For the $f = 2$ Hz simulation we reduced the time step to $\Delta t = T/32000$ to ensure that it is quite smaller than the relaxation time; this results in $\lambda/\Delta t \approx 45$.

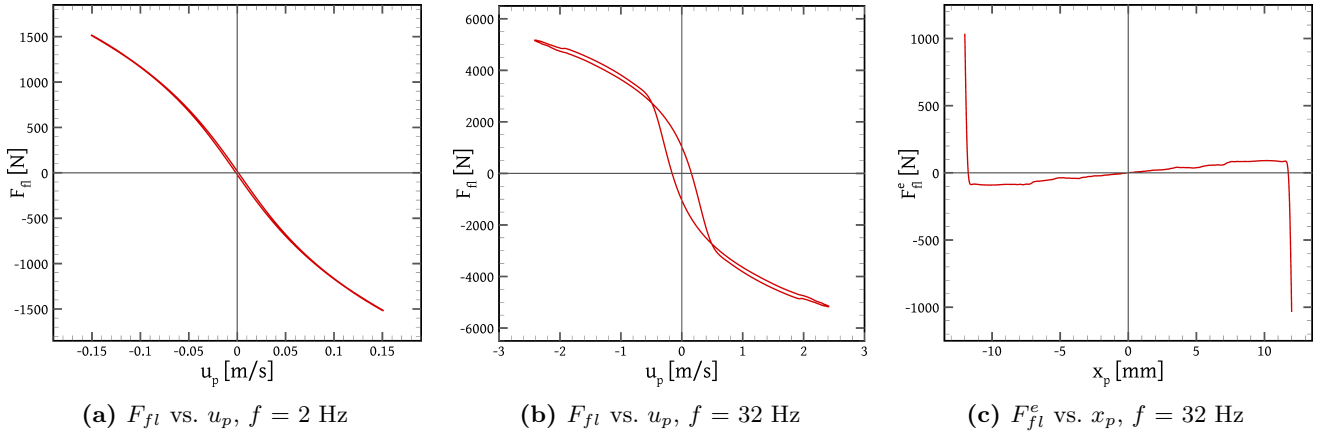


Figure 22: Plots (a) and (b): F_{fl} versus piston velocity for the IPTT-10 fluid, at oscillation frequencies of $f = 2$ Hz (a) and 32 Hz (b). Plot (c): F_{fl}^e versus piston displacement for the IPTT-10 fluid at $f = 32$ Hz.

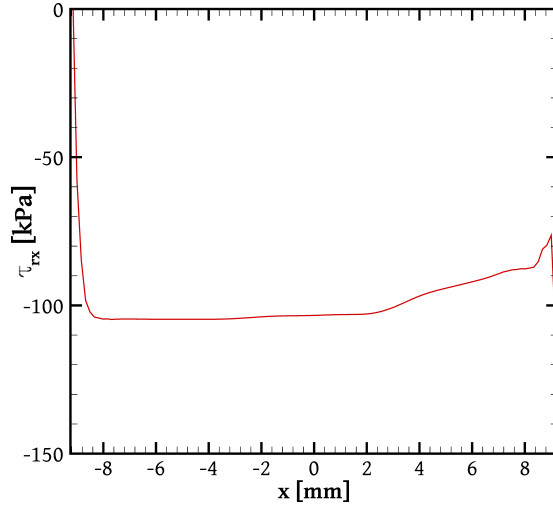


Figure 23: Distributions of the τ_{rx} stress component along the horizontal surface of the piston for the IPTT-10 fluid oscillating at $f = 32$ Hz, at a time instance when the piston is moving with maximum velocity towards the right.

expected. Concerning shear-thinning, comparison of the slope variations between Figs. 22a and 22b shows that it is significantly more pronounced in the $f = 32$ Hz case, as expected.

Figure 23 shows that in the $f = 32$ Hz case there does exist a substantial flow development length inside the gap, however it is smaller than that of the IPTT-100 fluid (Fig. 17). A comparison between Figs. 23 and 17 also shows that the stress in the IPTT-10 case is nearly 1.5 times that of the IPTT-100 case, which can be attributed to the weaker shear-thinning property of the IPTT-10 fluid. In fact a comparison between Figs. 22b and 13b shows that the IPTT-10 force is more than 2.5 times that of the IPTT-100 fluid at the same frequency. This is because the narrowing of the gap brings about a larger rise in the pressure component of F_{fl} (which is the dominant one, $O(h^{-3})$) than in the stress component ($O(h^{-2})$), as discussed above. In particular, Fig. 8 shows that for IPTT-100 the stress component is more than 10% of the total force, but for the IPTT-10 fluid the results showed that it is only 6%. Interestingly, even for the $f = 2$ Hz case the IPTT-10 force is still nearly twice that for IPTT-100 (Figs. 22a and 13b). We conclude that the difference in shear-thinning character between high- and low-viscosity oils is responsible for higher forces in the latter, under conditions that would produce similar forces had the viscosity been constant. The IPTT-100 and IPTT-10 fluids will produce similar forces at frequencies low enough for shear rates to drop below the onset of shear-thinning for the IPTT-100 fluid. Overall then, utilization of high-viscosity silicone oils can be beneficial in applications where it is desirable to moderate the variation of the damper force with oscillation frequency.

5. Conclusions

The present study investigated the operation of a silicone oil fluid damper of a common design under a forced sinusoidal piston displacement through numerical simulations. In order to relate the damper behaviour to the fluid rheology, three different rheological models were used to describe the behaviour of the fluid: the Newtonian, Carreau-Yasuda, and Phan-Thien & Tanner models. Their parameters were selected such as to describe the behaviour of high-viscosity silicone oil.

Due to the high viscosity, the Newtonian model predicts creeping, quasi-steady flow without any hysteresis. Its force-displacement plots are perfectly elliptical, and its force-velocity plots are straight lines.

The Carreau-Yasuda model defines a shear-thinning behaviour that predicts much lower force levels than in the Newtonian case. It also makes the force-displacement loops more rectangular, i.e. it predicts relatively constant force over most of the piston stroke, and makes the force roughly proportional to the piston velocity raised to a power less than one. Furthermore, at high frequencies, where shear-thinning is intense enough to lower viscous stresses to the point that fluid inertia is not negligible any more, the Carreau-Yasuda model predicts some inertial hysteresis, i.e. that the force is greater when the piston is accelerating than when it is decelerating, at a given piston displacement or velocity.

Finally, the PTT model in addition to describing a shear-thinning behaviour also describes the elastic behaviour of the fluid. This is the most complete model among those considered and in addition to the features predicted also by the CY model it predicts an elastic hysteresis where the force has an elastic component that pushes the piston away from the extreme positions, like in a spring. Furthermore, a PTT fluid that exhibits the same shear-thinning as a CY fluid was seen to produce lower force levels than the latter, especially the higher the frequency or fluid elasticity. This was shown to arise from elasticity, which delays the development of a fully developed velocity profile in the piston-cylinder gap.

Among these three rheological models, the one whose predictions qualitatively match better the experimental results available in the literature (e.g. [14–16]) is the PTT viscoelastic model. The Newtonian model is completely inaccurate, while the CY model fails to predict the stiffness characteristics of the damper behaviour and cannot account for a further force reduction due to elasticity. Thus it is shown that fluid elasticity suffices to induce stiffness in the damper behaviour even if fluid compressibility is not accounted for. The PTT predictions resemble also the experimental results concerning magnetorheological dampers [24, 3, 20, 8, 25], which is explained by the fact that shear-thinning is in some respects similar to plasticity. For more accurate modelling of MR dampers an elastoviscoplastic constitutive equation should be used instead.

The present results also reveal that, since the viscoelastic flow in the critical region of the gap varies along the gap length, the accuracy obtainable by simplified studies that assume one-dimensional flow in that region is limited. Full two-dimensional (axisymmetric) simulations are necessary in order to obtain an accurate understanding of the flow.

To the best of our knowledge this is the first numerical study of the flow in a damper which models the fluid through a viscoelastic constitutive equation, and it has shown that numerical simulation can be a valuable aid in damper research if the fluid physics is modelled accurately. Future studies can incorporate temperature changes due to viscous dissipation, temperature-dependent fluid rheology, fluid compressibility, and plasticity (for MR dampers).

Acknowledgements

This research was funded by the LIMMAT Foundation under the Project “MuSiComPS”.

Appendix A Steady shear flow of PTT fluids

In steady shear flow the velocity vector is given by $\underline{u} = (\dot{\gamma} x_2, 0, 0)$, where $\dot{\gamma}$ is the imposed shear rate, while the pressure gradient is zero (as in Couette flow between parallel plates, where the fluid flows in the x_1 direction while the plate normal vectors are aligned with the x_2 direction). The flow is steady and one-dimensional so that the only (possibly) non-zero partial derivatives of the flow variables are those with respect to the x_2 direction. Under these conditions the first component of the momentum equation (7)

implies that the stress component τ_{12} is constant ($\partial\tau_{12}/\partial x_2 = 0$). The (2,2) component of the constitutive equation (9) gives $\tau_{22} = 0$, while the components (1,1) and (1,2) reduce to the following:

$$Y(\text{tr}(\underline{\tau})) \tau_{11} = 2\lambda \tau_{12} \dot{\gamma} \quad (\text{A.1})$$

$$Y(\text{tr}(\underline{\tau})) \tau_{12} = \eta_0 \dot{\gamma} \quad (\text{A.2})$$

The explicit form of the function Y has not yet been substituted, so that the above equations hold for both the linear and the exponential PTT models. Next, Eq. (A.1) is divided by Eq. (A.2) to get

$$\tau_{11} = \frac{2\lambda}{\eta_0} \tau_{12}^2 \quad (\text{A.3})$$

Noting that $\text{tr}(\underline{\tau}) = \tau_{11} + \tau_{22} + \tau_{33} = \tau_{11}$ we can substitute the above equation into (A.2) to obtain an equation with only one unknown, τ_{12} :

$$Y\left(\frac{2\lambda}{\eta_0} \tau_{12}^2\right) \tau_{12} = \eta_0 \dot{\gamma} \quad (\text{A.4})$$

In the linear PTT case ($Y(x) = 1 + (\epsilon\lambda/\eta_0)x$) the above equation becomes

$$\tau_{12} + \frac{2\epsilon\lambda^2}{\eta_0^2} \tau_{12}^3 = \eta_0 \dot{\gamma} \quad (\text{A.5})$$

which is a cubic polynomial equation whose analytic solution can be found in [39]. In the exponential PTT case ($Y(x) = \exp((\epsilon\lambda/\eta_0)x)$) Eq. (A.4) becomes

$$\exp\left(\frac{2\epsilon\lambda^2}{\eta_0^2} \tau_{12}^2\right) \tau_{12} = \eta_0 \dot{\gamma} \quad (\text{A.6})$$

This seems more unwieldy than (A.5) but it turns out that it also has an analytic solution (although it does not seem to be reported in the literature). For simplicity, let $2\epsilon\lambda^2/\eta_0^2 \equiv a > 0$, $\tau_{12} \equiv x$ and $\eta_0\dot{\gamma} \equiv b > 0$ so that the equation becomes

$$e^{ax^2} x = b \quad \Rightarrow \quad e^{2ax^2} x^2 = b^2 \quad \Rightarrow \quad 2ax^2 e^{2ax^2} = 2ab^2 \quad \Rightarrow \quad 2ax^2 = W(2ab^2)$$

where W is the Lambert W function [80], i.e. the inverse function of $f(x) = xe^x$: $xe^x = y \Leftrightarrow x = W(y)$. Solving for $x \equiv \tau_{12}$ we obtain⁷

$$\tau_{12}(\dot{\gamma}) = \sqrt{\frac{\eta_0^2 W(4\epsilon\lambda^2\dot{\gamma}^2)}{4\epsilon\lambda^2}} \quad (\text{A.7})$$

Having obtained the shear stress τ_{12} from (A.5) or (A.7), the steady shear viscosity $\eta(\dot{\gamma}) = \tau_{12}(\dot{\gamma})/\dot{\gamma}$ is plotted in Fig. 2 for the selected models. It may be seen from Eq. (A.5) that in the limit of very small shear rates $\dot{\gamma}$ the stress τ_{12} also becomes very small and since in this case $\tau_{12}^3 \ll \tau_{12}$, Eq. (A.5) asymptotically reduces to $\tau_{12} = \eta_0\dot{\gamma}$. Thus η_0 is the zero-shear viscosity, $\eta_0 = \lim \eta(\dot{\gamma})$ as $\dot{\gamma} \rightarrow 0$. The same can be said of the exponential PTT model. In fact, expanding the exponential in Eq. (A.6) in a Maclaurin series with respect to τ_{12} and discarding all terms of this series except the first two, we obtain Eq. (A.5). The discarded terms contain higher powers of τ_{12} which will be negligible if $\dot{\gamma}$ is small enough (which implies small τ_{12}). Thus at small shear rates the linear and exponential PTT models become equivalent.

Finally, we note that in both Eq. (A.5) and (A.6) (or (A.7)) the individual values of λ and ϵ do not make a difference, but it is the product $\epsilon\lambda^2$ that determines the solution. Thus even if λ and ϵ of two different PTT fluids differ by orders of magnitude, if the product $\epsilon\lambda^2$ is the same for both fluids then their $\tau_{12}(\dot{\gamma})$ curves will coincide in a diagram such as that of Fig. 2.

⁷The Lambert W function is double-valued on the interval $(-1/e, 0)$, but here $2ab^2 > 0$ and there is only one branch to follow.

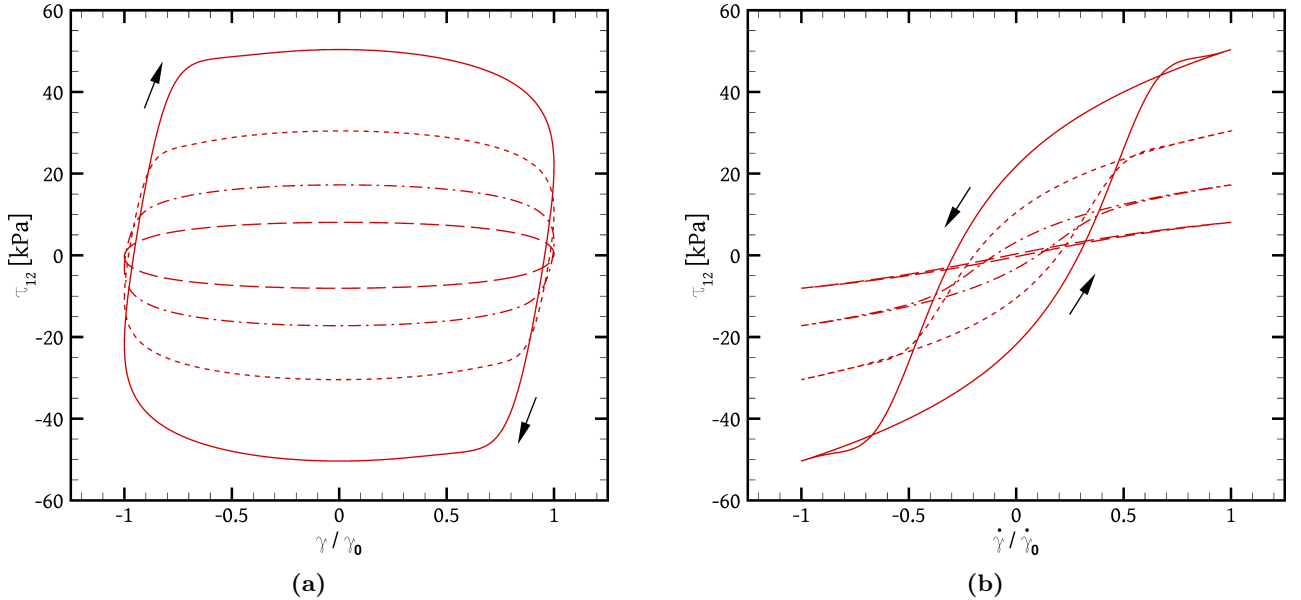


Figure 24: Diagrams of shear stress versus normalised shear (a) or shear rate (b) for simulations of LAOS flow of the IPTT-100 fluid. The oscillation frequencies are $f = 0.5$ (long dashes), 2 (dash-dot), 8 (short dashes) and 32 (continuous line) Hz, and the corresponding shear rate amplitudes $\dot{\gamma}_0$ are equal to the respective $\dot{\gamma}_c$ values of Table 3.

Appendix B LAOS flow of PTT fluids

For unsteady flow of a PTT fluid between parallel plates, driven by the motion of the top plate, under the assumption that the distance between the plates is so small that fluid inertia is negligible and the velocity varies linearly as $\underline{u} = (\dot{\gamma}(t)x_2, 0, 0)$, the governing equations contain an additional time derivative compared to the steady-state Eqs. (A.1) – (A.2):

$$\lambda \frac{\partial \tau_{11}}{\partial t} + Y(\text{tr}(\underline{\underline{\tau}})) \tau_{11} = 2\lambda \tau_{12} \dot{\gamma} \quad (\text{B.8})$$

$$\lambda \frac{\partial \tau_{12}}{\partial t} + Y(\text{tr}(\underline{\underline{\tau}})) \tau_{12} = \eta_0 \dot{\gamma} \quad (\text{B.9})$$

A particular such transient flow which is commonly used in rheometry and shares some similarities with the flow in a damper that is the topic of this paper, is Large Amplitude Oscillatory Flow (LAOS) [67], where the moving plate oscillates so that $\dot{\gamma}(t) = \dot{\gamma}_0 \cos(\omega t)$ where $\dot{\gamma}_0$ is the maximum shear rate during an oscillation and ω is the angular frequency. In Fig. 24 we plot Lissajous-Bowditch curves, i.e. curves of shear stress versus strain (Fig. 24a, where the strain is given by $\gamma(t) = \int_0^t \dot{\gamma} dt = \dot{\gamma}_0 \sin(\omega t)$, $\gamma_0 = \dot{\gamma}_0/\omega$) or strain rate (Fig. 24b) for the IPTT-100 fluid for $\omega = 2\pi f$, $f = 0.5, 2, 8$ and 32 Hz and $\dot{\gamma}_0$ being equal to the corresponding $\dot{\gamma}_c$ values of Table 3. These plots are very similar to the force-displacement and force velocity diagrams of the damper simulations, such as Figs. 12 and 13b (only that they are travelled in opposite senses because the force plots record the force on the moving wall, while the LAOS plots record the stress on the stationary wall). These LAOS plots reveal fluid properties such as elasticity and shear-thinning in the same way that the force diagrams of the damper simulations do. Nevertheless, there are significant differences between the two types of flow, as noted in the text. The plots of Fig. 24 do not account for inertia, since it has been omitted from the governing equations; to account for it, one would have to solve, instead of the system of ordinary differential equations (B.8) – (B.9), a system of one-dimensional partial differential equations that includes the momentum equation, where stress and inertia vary in the direction perpendicular to the plates. It is interesting to notice in Fig. 24b that in the $f = 32$ Hz case as the shear rate approaches its maximum magnitude there appear a pair of secondary loops where the hysteresis is reversed, which is something that inertia can also cause (e.g. Figs. 13a, 20b) but in Fig. 24b it is caused by strong nonlinearities in the elastic behaviour of the fluid [81].

References

References

- [1] M. C. Constantinou and M. D. Symans, “Experimental study of seismic response of buildings with supplemental fluid dampers,” *The Structural Design of Tall Buildings*, vol. 2, pp. 93–132, jun 1993.
- [2] D. Konstantinidis, N. Makris, and J. M. Kelly, “In-situ condition assessment of seismic fluid dampers: experimental studies and challenges,” *Meccanica*, vol. 50, no. 2, pp. 323–340, 2015.
- [3] G. Yao, F. Yap, G. Chen, W. Li, and S. Yeo, “MR damper and its application for semi-active control of vehicle suspension system,” *Mechatronics*, vol. 12, pp. 963–973, sep 2002.
- [4] Q.-H. Nguyen and S.-B. Choi, “Optimal design of MR shock absorber and application to vehicle suspension,” *Smart Materials and Structures*, vol. 18, p. 035012, feb 2009.
- [5] A. Rittweger, J. Albus, E. Hornung, H. Öry, and P. Mourey, “Passive damping devices for aerospace structures,” *Acta Astronautica*, vol. 50, pp. 597–608, may 2002.
- [6] A. Seleemah and M. C. Constantinou, “Investigation of seismic response of buildings with linear and nonlinear fluid viscous dampers,” Tech. Rep. NCEER-97-0004, National Center for Earthquake Engineering Research, 1997.
- [7] N. Makris and M. C. Constantinou, “Fractional-derivative maxwell model for viscous dampers,” *Journal of Structural Engineering*, vol. 117, pp. 2708–2724, sep 1991.
- [8] D. H. Wang and W. H. Liao, “Magnetorheological fluid dampers: a review of parametric modelling,” *Smart Materials and Structures*, vol. 20, p. 023001, jan 2011.
- [9] L.-Y. Lu, G.-L. Lin, and M.-H. Shih, “An experimental study on a generalized Maxwell model for nonlinear viscoelastic dampers used in seismic isolation,” *Engineering Structures*, vol. 34, pp. 111–123, jan 2012.
- [10] C. C. Currie and B. F. Smith, “Flow characteristics of organopolysiloxane fluids and greases,” *Industrial & Engineering Chemistry*, vol. 42, pp. 2457–2462, dec 1950.
- [11] P. Longin, C. Verdier, and M. Piau, “Dynamic shear rheology of high molecular weight polydimethylsiloxanes: comparison of rheometry and ultrasound,” *Journal of Non-Newtonian Fluid Mechanics*, vol. 76, pp. 213–232, 1998.
- [12] Z. Kokuti, K. van Gruijthuisen, M. Jenei, G. Toth-Molnar, A. Czirjak, J. Kokavecz, P. Ailer, L. Palkovics, A. Volker, and G. Szabo, “High-frequency rheology of a high viscosity silicone oil using diffusing wave spectroscopy,” *Applied Rheology*, vol. 24, no. 6, p. 63984, 2014.
- [13] C. J. Black and N. Makris, “Viscous heating of fluid dampers under small and large amplitude motions: Experimental studies and parametric modeling,” *Journal of Engineering Mechanics*, vol. 133, pp. 566–577, may 2007.
- [14] C.-Y. Hou, “Fluid dynamics and behavior of nonlinear viscous fluid dampers,” *Journal of Structural Engineering*, vol. 134, no. 1, pp. 56–63, 2008.
- [15] H.-B. Yun, F. Tasbighoo, S. Masri, J. Caffrey, R. Wolfe, N. Makris, and C. Black, “Comparison of modeling approaches for full-scale nonlinear viscous dampers,” *Journal of Vibration and Control*, vol. 14, pp. 51–76, jan 2008.
- [16] S. Jiao, J. Tian, H. Zheng, and H. Hua, “Modeling of a hydraulic damper with shear thinning fluid for damping mechanism analysis,” *Journal of Vibration and Control*, vol. 23, pp. 3365–3376, feb 2017.
- [17] K. Yasuda, R. Armstrong, and R. Cohen, “Shear flow properties of concentrated solutions of linear and star branched polystyrenes,” *Rheologica Acta*, vol. 20, no. 2, pp. 163–178, 1981.

- [18] J. Sun, S. Jiao, X. Huang, and H. Hua, "Investigation into the impact and buffering characteristics of a non-Newtonian fluid damper: Experiment and simulation," *Shock and Vibration*, vol. 2014, 2014. Article ID 170464.
- [19] N. Makris, S. A. Burton, D. Hill, and M. Jordan, "Analysis and design of ER damper for seismic protection of structures," *Journal of Engineering Mechanics*, vol. 122, no. 10, pp. 1003–1011, 1996.
- [20] X. Wang and F. Gordaninejad, "Flow analysis and modeling of field-controllable, electro-and magnetorheological fluid dampers," *Journal of Applied Mechanics*, vol. 74, no. 1, pp. 13–22, 2007.
- [21] R. Fattal and R. Kupferman, "Time-dependent simulation of viscoelastic flows at high weissenberg number using the log-conformation representation," *Journal of Non-Newtonian Fluid Mechanics*, vol. 126, pp. 23–37, feb 2005.
- [22] A. Syrakos, Y. Dimakopoulos, G. C. Georgiou, and J. Tsamopoulos, "Viscoplastic flow in an extrusion damper," *Journal of Non-Newtonian Fluid Mechanics*, vol. 232, pp. 102–124, jun 2016.
- [23] N. Phan-Thien and R. I. Tanner, "A new constitutive equation derived from network theory," *Journal of Non-Newtonian Fluid Mechanics*, vol. 2, pp. 353–365, jul 1977.
- [24] R. A. Snyder, G. M. Kamath, and N. M. Wereley, "Characterization and analysis of magnetorheological damper behavior under sinusoidal loading," *AIAA Journal*, vol. 39, pp. 1240–1253, jan 2001.
- [25] Z. Parlak and T. Engin, "Time-dependent CFD and quasi-static analysis of magnetorheological fluid dampers with experimental validation," *International Journal of Mechanical Sciences*, vol. 64, no. 1, pp. 22–31, 2012.
- [26] G. W. Rodgers, J. G. Chase, J. B. Mander, N. C. Leach, and C. S. Denmead, "Experimental development, tradeoff analysis and design implementation of high force-to-volume damping technology," *Bulletin of the New Zealand National Society for Earthquake Engineering*, vol. 40, no. 2, pp. 35–48, 2007.
- [27] N. M. Wereley and L. Pang, "Nondimensional analysis of semi-active electrorheological and magnetorheological dampers using approximate parallel plate models," *Smart Materials and Structures*, vol. 7, no. 5, p. 732, 1998.
- [28] Q.-H. Nguyen and S.-B. Choi, "Dynamic modeling of an electrorheological damper considering the unsteady behavior of electrorheological fluid flow," *Smart Materials and Structures*, vol. 18, no. 5, p. 055016, 2009.
- [29] N. Makris, "Viscous heating of fluid dampers. I: Small-amplitude motions," *Journal of Engineering Mechanics*, vol. 124, pp. 1210–1216, nov 1998.
- [30] N. Makris, Y. Roussos, A. S. Whittaker, and J. M. Kelly, "Viscous heating of fluid dampers. II: Large-amplitude motions," *Journal of Engineering Mechanics*, vol. 124, no. 11, pp. 1217–1223, 1998.
- [31] A. J. Barlow, G. Harrison, and J. Lamb, "Viscoelastic relaxation of polydimethylsiloxane liquids," *Proceedings of the Royal Society A: Mathematical, Physical and Engineering Sciences*, vol. 282, pp. 228–251, nov 1964.
- [32] F. A. Morrison, *Understanding Rheology*. Oxford University Press, 2001.
- [33] N. Phan-Thien, "A nonlinear network viscoelastic model," *Journal of Rheology*, vol. 22, pp. 259–283, jun 1978.
- [34] K. Foteinopoulou, V. G. Mavrantzas, and J. Tsamopoulos, "Numerical simulation of bubble growth in newtonian and viscoelastic filaments undergoing stretching," *Journal of Non-Newtonian Fluid Mechanics*, vol. 122, pp. 177–200, sep 2004.

- [35] Y. Dimakopoulos and J. Tsamopoulos, “On the transient coating of a straight tube with a viscoelastic material,” *Journal of Non-Newtonian Fluid Mechanics*, vol. 159, pp. 95–114, jun 2009.
- [36] J. Papaioannou, A. Giannousakis, Y. Dimakopoulos, and J. Tsamopoulos, “Bubble deformation and growth inside viscoelastic filaments undergoing very large extensions,” *Industrial & Engineering Chemistry Research*, vol. 53, pp. 7548–7569, may 2014.
- [37] D. Pettas, G. Karapetsas, Y. Dimakopoulos, and J. Tsamopoulos, “On the origin of extrusion instabilities: Linear stability analysis of the viscoelastic die swell,” *Journal of Non-Newtonian Fluid Mechanics*, vol. 224, pp. 61–77, oct 2015.
- [38] D. Fraggedakis, M. Pavlidis, Y. Dimakopoulos, and J. Tsamopoulos, “On the velocity discontinuity at a critical volume of a bubble rising in a viscoelastic fluid,” *Journal of Fluid Mechanics*, vol. 789, pp. 310–346, jan 2016.
- [39] J. Azaiez, R. Guénette, and A. At-Kadi, “Numerical simulation of viscoelastic flows through a planar contraction,” *Journal of Non-Newtonian Fluid Mechanics*, vol. 62, pp. 253–277, feb 1996.
- [40] R. Poole, “The Deborah and Weissenberg numbers,” *British Soc. Rheol. Rheol. Bull*, vol. 53, pp. 32–39, 2012.
- [41] G. K. Batchelor, *An introduction to fluid dynamics*. Cambridge university press, 2000. Pages 224–227.
- [42] Q. He and X.-P. Wang, “Numerical study of the effect of Navier slip on the driven cavity flow,” *ZAMM-Journal of Applied Mathematics and Mechanics*, vol. 89, no. 10, pp. 857–868, 2009.
- [43] J. Koplik and J. R. Banavar, “Corner flow in the sliding plate problem,” *Physics of Fluids*, vol. 7, no. 12, pp. 3118–3125, 1995.
- [44] T. Qian and X.-P. Wang, “Driven cavity flow: from molecular dynamics to continuum hydrodynamics,” *Multiscale Modeling & Simulation*, vol. 3, no. 4, pp. 749–763, 2005.
- [45] S. G. Hatzikiriakos, “Slip mechanisms in complex fluid flows,” *Soft Matter*, vol. 11, no. 40, pp. 7851–7856, 2015.
- [46] S. G. Hatzikiriakos, “Wall slip of molten polymers,” *Progress in Polymer Science*, vol. 37, no. 4, pp. 624–643, 2012.
- [47] L. A. Archer, “Wall slip: Measurement and modeling issues,” in *Polymer processing instabilities: Control and understanding* (S. G. Hatzikiriakos and K. B. Migler, eds.), ch. 4, pp. 73–120, Marcel Dekker, 2005.
- [48] G. Karapetsas and J. Tsamopoulos, “Transient squeeze flow of viscoplastic materials,” *Journal of Non-Newtonian Fluid Mechanics*, vol. 133, pp. 35–56, 2006.
- [49] A. Syrakos and A. Goulas, “Estimate of the truncation error of finite volume discretization of the Navier-Stokes equations on colocated grids,” *International Journal for Numerical Methods in Fluids*, vol. 50, no. 1, pp. 103–130, 2006.
- [50] A. Syrakos and A. Goulas, “Finite volume adaptive solutions using SIMPLE as smoother,” *International Journal for Numerical Methods in Fluids*, vol. 52, pp. 1215–1245, 2006.
- [51] M. Pavlidis, Y. Dimakopoulos, and J. Tsamopoulos, “Steady viscoelastic film flow over 2d topography: I. the effect of viscoelastic properties under creeping flow,” *Journal of Non-Newtonian Fluid Mechanics*, vol. 165, pp. 576–591, jun 2010.
- [52] Y. Dimakopoulos and J. Tsamopoulos, “A quasi-elliptic transformation for moving boundary problems with large anisotropic deformations,” *Journal of Computational Physics*, vol. 192, pp. 494–522, dec 2003.

- [53] N. Chatzidai, A. Giannousakis, Y. Dimakopoulos, and J. Tsamopoulos, “On the elliptic mesh generation in domains containing multiple inclusions and undergoing large deformations,” *Journal of Computational Physics*, vol. 228, pp. 1980–2011, apr 2009.
- [54] A. Syrakos, S. Varchanis, Y. Dimakopoulos, A. Goulas, and J. Tsamopoulos, “A critical analysis of some popular methods for the discretisation of the gradient operator in finite volume methods,” *Physics of Fluids*, vol. 29, p. 127103, dec 2017.
- [55] C. M. Rhie and W. L. Chow, “Numerical study of the turbulent flow past an airfoil with trailing edge separation,” *AIAA Journal*, vol. 21, pp. 1525–1532, nov 1983.
- [56] P. Oliveira, F. Pinho, and G. Pinto, “Numerical simulation of non-linear elastic flows with a general collocated finite-volume method,” *Journal of Non-Newtonian Fluid Mechanics*, vol. 79, pp. 1–43, sep 1998.
- [57] H. M. Matos, M. A. Alves, and P. J. Oliveira, “New formulation for stress calculation: Application to viscoelastic flow in a T-junction,” *Numerical Heat Transfer, Part B: Fundamentals*, vol. 56, pp. 351–371, jan 2009.
- [58] A. Afonso, M. Oliveira, P. Oliveira, M. Alves, and F. Pinho, “The finite-volume method in computational rheology,” in *Finite-Volume Methods - Powerful Means of Engineering Design*, ch. 7, pp. 141–170, In-Tech Open Publishers, 2012.
- [59] R. Fattal and R. Kupferman, “Constitutive laws for the matrix-logarithm of the conformation tensor,” *Journal of Non-Newtonian Fluid Mechanics*, vol. 123, pp. 281–285, nov 2004.
- [60] A. Afonso, P. Oliveira, F. Pinho, and M. Alves, “The log-conformation tensor approach in the finite-volume method framework,” *Journal of Non-Newtonian Fluid Mechanics*, vol. 157, pp. 55–65, mar 2009.
- [61] M. A. Alves, P. J. Oliveira, and F. T. Pinho, “A convergent and universally bounded interpolation scheme for the treatment of advection,” *International Journal for Numerical Methods in Fluids*, vol. 41, no. 1, pp. 47–75, 2003.
- [62] A. Sidi, “Review of two vector extrapolation methods of polynomial type with applications to large-scale problems,” *Journal of Computational Science*, vol. 3, pp. 92–101, 2012.
- [63] P. Saramito, “On a modified non-singular log-conformation formulation for Johnson–Segalman viscoelastic fluids,” *Journal of Non-Newtonian Fluid Mechanics*, vol. 211, pp. 16–30, sep 2014.
- [64] R. Sousa, R. Poole, A. Afonso, F. Pinho, P. Oliveira, A. Morozov, and M. Alves, “Lid-driven cavity flow of viscoelastic liquids,” *Journal of Non-Newtonian Fluid Mechanics*, vol. 234, pp. 129–138, aug 2016.
- [65] S. Dalal, G. Tomar, and P. Dutta, “Numerical study of driven flows of shear thinning viscoelastic fluids in rectangular cavities,” *Journal of Non-Newtonian Fluid Mechanics*, vol. 229, pp. 59–78, mar 2016.
- [66] P. J. Oliveira, “Method for time-dependent simulations of viscoelastic flows: vortex shedding behind cylinder,” *Journal of Non-Newtonian Fluid Mechanics*, vol. 101, pp. 113–137, nov 2001.
- [67] K. Hyun, M. Wilhelm, C. O. Klein, K. S. Cho, J. G. Nam, K. H. Ahn, S. J. Lee, R. H. Ewoldt, and G. H. McKinley, “A review of nonlinear oscillatory shear tests: Analysis and application of large amplitude oscillatory shear (LAOS),” *Progress in Polymer Science*, vol. 36, pp. 1697–1753, dec 2011.
- [68] M. A. Alves and R. J. Poole, “Divergent flow in contractions,” *Journal of Non-Newtonian Fluid Mechanics*, vol. 144, pp. 140–148, jul 2007.
- [69] P. Sousa, P. Coelho, M. Oliveira, and M. Alves, “Three-dimensional flow of Newtonian and Boger fluids in square–square contractions,” *Journal of Non-Newtonian Fluid Mechanics*, vol. 160, pp. 122–139, aug 2009.

- [70] P. Sousa, P. Coelho, M. Oliveira, and M. Alves, “Effect of the contraction ratio upon viscoelastic fluid flow in three-dimensional square–square contractions,” *Chemical Engineering Science*, vol. 66, pp. 998–1009, mar 2011.
- [71] A. M. Afonso, P. J. Oliveira, F. T. Pinho, and M. A. Alves, “Dynamics of high-Deborah-number entry flows: a numerical study,” *Journal of Fluid Mechanics*, vol. 677, pp. 272–304, apr 2011.
- [72] R. Comminal, J. H. Hattel, M. A. Alves, and J. Spangenberg, “Vortex behavior of the Oldroyd-B fluid in the 4-1 planar contraction simulated with the streamfunction–log-conformation formulation,” *Journal of Non-Newtonian Fluid Mechanics*, vol. 237, pp. 1–15, nov 2016.
- [73] M. R. Hashemi, M. T. Manzari, and R. Fatehi, “Non-linear stress response of non-gap-spanning magnetic chains suspended in a newtonian fluid under oscillatory shear test: A direct numerical simulation,” *Physics of Fluids*, vol. 29, p. 107106, oct 2017.
- [74] K. S. Cho, K. Hyun, K. H. Ahn, and S. J. Lee, “A geometrical interpretation of large amplitude oscillatory shear response,” *Journal of Rheology*, vol. 49, pp. 747–758, may 2005.
- [75] P. Saramito and J. Piau, “Flow characteristics of viscoelastic fluids in an abrupt contraction by using numerical modeling,” *Journal of Non-Newtonian Fluid Mechanics*, vol. 52, pp. 263–288, may 1994.
- [76] M. A. Alves, P. J. Oliveira, and F. T. Pinho, “Benchmark solutions for the flow of Oldroyd-B and PTT fluids in planar contractions,” *Journal of Non-Newtonian Fluid Mechanics*, vol. 110, pp. 45–75, feb 2003.
- [77] M. S. Oliveira, P. J. Oliveira, F. T. Pinho, and M. A. Alves, “Effect of contraction ratio upon viscoelastic flow in contractions: The axisymmetric case,” *Journal of Non-Newtonian Fluid Mechanics*, vol. 147, pp. 92–108, nov 2007.
- [78] A. E. Likhtman and T. C. B. McLeish, “Quantitative theory for linear dynamics of linear entangled polymers,” *Macromolecules*, vol. 35, pp. 6332–6343, jul 2002.
- [79] R. P. Wool, “Polymer entanglements,” *Macromolecules*, vol. 26, pp. 1564–1569, mar 1993.
- [80] R. M. Corless, G. H. Gonnet, D. E. Hare, D. J. Jeffrey, and D. E. Knuth, “On the Lambert W function,” *Advances in Computational Mathematics*, vol. 5, pp. 329–359, 1996.
- [81] R. H. Ewoldt and G. H. McKinley, “On secondary loops in LAOS via self-intersection of lissajous–bowditch curves,” *Rheologica Acta*, vol. 49, pp. 213–219, dec 2010.